# Malaysian Journal of Analytical Sciences (MJAS) Published by Malaysian Analytical Sciences Society

## THE ELECTROCHEMICAL BEHAVIOUR OF Au-PEDOT/rGO MODIFIED ELECTRODE IN URIC ACID

(Sifat Elektrokimia Elektrod Bermodifikasi Komposit Au-PEDOT/rGO dalam Asid Urik)

Farhanini Yusoff<sup>1</sup>\*, Mohd Faris Rosdidi<sup>1</sup>, Azleen Rashidah Mohd Rosli<sup>1</sup>, Syara Kassim<sup>2</sup>, Noor Aniza Harun<sup>2</sup>, Noorashikin Md Saleh<sup>3</sup>

<sup>1</sup>Faculty of Science and Marine Environment

<sup>2</sup>Advanced Nano Materials (ANoMa) Research Group, Faculty of Science and Marine Environment

Universiti Malaysia Terengganu, 21030 Kuala Nerus, Terengganu, Malaysia

<sup>3</sup>Research Centre for Sustainable Process Technology, Department of Chemical Engineering,

Faculty of Engineering and Built Environment,

Universiti Kebangsaan Malaysia, 43600 UKM Bangi, Selangor, Malaysia

\*Corresponding author: farhanini@umt.edu.my

Received: 28 March 2021; Accepted: 23 May 2021; Published: 27 June 2021

#### **Abstract**

The development of gold nanoparticle/poly(3,4-ethylene dioxythiophene)/reduced graphene oxide (denoted as Au-PEDOT/rGO) sensor is necessary for the detection of UA as the irregular amount of UA in the human body may cause several diseases such as gout, heart disease, kidney stone and hypertension. In this work, Au-PEDOT/rGO nanocomposite was synthesized by a facile chemical technique. The morphology, composition, and structure of Au-PEDOT/rGO composite were confirmed by FTIR, SEM, and XRD characterization. FTIR spectrum showed the presence of C-O-C stretching and C-S stretching of the thiophene ring. The attachment of Au with PEDOT and rGO was confirmed by SEM. XRD analysis showed the presence of Au(111), Au(200), Au(220), Au(311) and Au(222) corresponding to Au-PEDOT/rGO composite. This proved that Au-PEDOT/rGO has been successfully synthesized. The electrochemical behavior of Au-PEDOT/rGO/GCE was evaluated by cyclic voltammetry (CV) in 1.0 M KCl with 5 mM K4[Fe(CN)6] and the results demonstrated that Au-PEDOT/rGO/GCE has a better electrical conductivity for detection of UA in the real sample. DPV measurements showed a linear relationship between oxidation peak current and concentration of UA in phosphate buffer (pH 7) over the concentration range 0.10 μM until 25.0 μM. The limit of detection of UA is 0.05 μM, and the limit of quantification of UA is 0.22 μM. Thus, Au-PEDOT/rGO electrode composite is a worthy alternative for the detection of UA in human's urine.

Keywords: conducting polymer, gold nanoparticles, reduced graphene oxide, uric acid

#### Abstrak

Pembangunan sensor buat zarah nano aurum/poli(3,4-etilenadioxitiofena/grafin oksida terturun (dilabel sebagai Au-PEDOT/rGO) adalah diperlukan untuk pengesanan UA kerana jumlah UA yang tidak normal dalam tubuh manusia boleh menyebabkan beberapa kondisi penyakit seperti gout, penyakit jantung, batu ginjal dan darah tinggi. Dalam kajian ini, komposit nano Au-PEDOT/rGO

### Farhanini et al: THE ELECTROCHEMICAL BEHAVIOUR OF Au-PEDOT/rGO MODIFIED ELECTRODE IN URIC ACID

telah disinthesis melalui teknik kimia mudah. Morfologi, komposisi, dan struktur komposit Au-PEDOT/rGO telah disahkan melalui teknik pencirian FTIR, SEM, dan XRD. Spektrum FTIR menunjukkan kehadiran regangan C-O-C dan regangan C-S bagi ikatan tiofena manakala penggabungan Au kepada lembaran PEDOT dan rGO telah dibuktikan melalui SEM. Analisis XRD menunjukkan kehadiran Au(111), Au(200), Au(220), Au (311) dan Au(222) sepadan dengan komposit Au-PEDOT/rGO. Keputusan tersebut telah mengesahkan bahawa Au-PEDOT/rGO telah berjaya disintesis. Sifat elektrokimia Au-PEDOT/rGO telah dinilai melalui voltammetri berkitar (CV) di dalam 1.0 M KCl bersama dengan 5 mM K4[Fe(CN)6] dan hasil kajian menunjukkan bahawa Au-PEDOT/rGO memiliki konduksi elektrik yang bagus untuk pengesanan UA di dalam sample nyata. Analisis DPV menunjukkan hubungan linear antara puncak pengoksidaan arus dan kepekatan UA di dalam penimbal fosfat (pH 7) diantara julat kepekatan 0.10 μM hingga 25.0 μM. Had pengesanan yang diukur bagi UA ialah 0.05 μM manakala had pengukuran UA adalah 0.22 μM. Oleh itu, komposit Au-PEDOT/rGO merupakan alternatif yang berbaloi untuk mengesan UA dalam air kencing manusia.

Kata kunci: polimer pengalir, zarah nano aurum, grafin oksida terturun, asid urik

#### Introduction

Uric acid (UA) is a purine end product formed by xanthine dehydrogenase in humans, and it has been discovered to play a significant role in the physiology of living organisms [1]. The two types of purine are exogenous and endogenous. The exogenous pool of purine is related to diet and animal proteins, while the endogenous purine metabolism that produces UA is from the liver, intestines, and other body tissues [2]. In theory, UA has either benefit or drawback effect toward the human body depending on concentration intake. Hyperuricemia that refers to overproduction or underexcretion of UA can lead to serious health issues such as heart disease, kidney stone, and gout [3]. These diseases are linked to chronic diseases such as hypertension, diabetes, metabolic syndrome, and renal failure [4]. The most common clinical features of hyperuricemia are associated with crystallization and uric acid deposition in surrounding joints and tissues. However, the precise mechanism of tissue injury caused by uric acid remains indefinite. Overproduction of UA also causes oxidative stress. Thus, this detection of UA will benefit not only the field of clinical diagnosis but also the human health.

Several methods of sensing UA in the human body have been discovered over the past years such as High Performance Liquid Chromatography (HPLC) [5], enzymatic [6], electrochemical [7] and phosphortungstic acid deoxidizing methods [8]. However, the electrochemical method is most favorable due to its fast analysis, low detection limit, sensitivity, and also high in accuracy compared to the other methods. UA often coexists with the presence of ascorbic acid (AA), and

dopamine (DA) in the human urine sample and these substances are electrochemically active substances that will interfere in the process of UA detection [9]. Thus, electrode surface modification is an effective alternative to overcome these problems as the bare electrode is found to have challenges in separating the peak of interference substance [10].

Graphene which is a thin sheet of hexagonally arranged carbon has captivate significant attention because of its exclusive thermal, optical and also its electrical characteristics. Graphene undergoes oxidation and exfoliation forming graphene oxide, which contains some reactive oxygen [11]. The immensely improved graphene oxide's surface ability makes it easier to bind with other compounds due to the oxygen-containing group [12].

Meanwhile, poly(3,4-ethylene dioxythiophene), also known as PEDOT, is one of the electroactive polymers that is widely studied because of its stability in the environment and enormous conductivity of its polycationic form [13]. This polymer is used for numerous applications as it possesses a simple synthesis process, superior biocompatibility and relatively wide electrical conductivity [10,14]. Recently, researches on noble metal nanoparticles such as platinum, gold, and silver were actively conducted due to their properties in conductivity and electrocatalyticity [15]. Gold (Au) nanoparticle has good prospects in the application of the detection of electroactive species [16]. Its specific structure, low toxicity, and biocompatibility make it compatible in sensing application [17].

Herein, we reported an electrocatalyst of Au decorated PEDOT functionalized with rGO (Au-PEDOT/rGO) which was synthesized by the facile synthesis technique. Then, the modified electrode was prepared via the drop-casting of the composite onto the surface of a glassy carbon electrode (GCE). The performance of the electrode as an electrochemical sensor for the detection of UA was evaluated using Cyclic Voltammetry (CV). The unique Au-PEDOT/rGO sensor is revealed to have a wide linear response over the concentration range from 0.1 to 25.0 µM UA. Additionally, detection of UA in a human urine sample is found to exhibit high accuracy. This newly developed sensor is expected to offer high accuracy, high sensitivity with fast analysis towards the determination of UA.

#### **Materials and Methods**

#### **Materials**

3,4-ethylenedioxythiophene (EDOT), gold(III) chloride hydrate (HAuCl<sub>4</sub>), sodium borohydride (NaBH<sub>4</sub>), sodium nitrate (NaNO<sub>3</sub>), graphite, Uric acid (UA), ethanol absolute (EtOH), potassium chloride (KCl) and potassium hexacyanoferrate(II) 3-hydrate (K<sub>4</sub>Fe(CN)<sub>6</sub>) powder were purchased from Sigma-Aldrich, USA. Meanwhile, di-potassium hydrogen phosphate (K<sub>2</sub>HPO<sub>4</sub>), potassium dihydrogen phosphate (KH<sub>2</sub>PO<sub>4</sub>), potassium permanganate (KMnO<sub>4</sub>), and aluminium oxide (Al<sub>2</sub>O<sub>3</sub>) were purchased from Merck, Germany. The UA standard solution was prepared in the 0.1 M of phosphate buffer solution.

#### Synthesis of rGO

Graphene oxide (GO) was synthesized from graphite powder via a modified Hummer's method, which was previously reported by Kaur *et al.*, 2018 [18]. Then, 200 mg of GO solution from the previous product was added into 200 ml of deionized water (DI) and sonicated for 2 hours. Next, 66.8 μL of hydrazine hydrate was added into the mixture with ratio of 1:3 (hydrazine: GO). The beaker was immersed in an oil bath at 80°C under cooled condenser for 12 hours. The solution was then transferred into 50 mL centrifuge tube and centrifuged at 3500 rpm for 10 minutes. The supernatant from the centrifuge process was removed and EtOH was added into the centrifuge tube to further centrifuge the solution. This step was repeated for three times and product was

then washed with DI water to remove excess impurities. Lastly, the product was filtered by a vacuum pump and dried at 60°C for 12 hours.

#### Preparation of Au/rGO

About 4 mL of rGO was added into 25 mL of HAuCl<sub>4</sub> solution (0.2 mg mL<sup>-1</sup>). The mixture was stirred for 1 hour in order to encourage the interaction between the graphene surface with the gold ions. 0.2 mol/mL of sodium citrate was dropped gradually into the mixture. Next, the solution was heated at 80°C for 2 hours [19]. The solution was then transferred into 50 mL centrifuge tube for centrifugation process at 3500 rpm for 10 minutes. The supernatant was removed then EtOH was added and centrifuge at 3500 rpm for 10 minutes. After 3 times removal of the excess supernatant, the product was resuspended by washing with deionized water via centrifugation. The product was filtered by vacuum pump and dry in oven at 60°C for 12 hours.

#### Preparation of Au-PEDOT/rGO

Approximately 70 mL of 0.65 mM HAuCl<sub>4</sub> solution was added into the mixture of 5 mL ethanol solution and 22.5 mM EDOT while stirred at the normal room temperature. The formation of PEDOT was occurred when the mixture colour changes from black-colored solution to dark blue and AuCl<sub>4</sub>- ions as the oxidant was reduced to form Au nanparticles [10]. The reaction was then kept stir for 4 hours. Later, the 0.5 mg/mL rGO suspension was mixed into the solution and then, the mixture was sonicated for 2 hours in order to disperse the Au-PEDOT and rGO. Lastly, the obtained solution was centrifuged by transfer the solution into the centrifuge tube and washed with EtOH and distilled water repeatedly until a neutral pH.

#### Characterization of Au-PEDOT/rGO

The characterization of Au-PEDOT/rGO was determined by using Fourier Transform Infrared Spectrometer (FTIR) for determination of the functional group and Scanning Electron Microscopy (SEM) was used to study the surface morphology and structure of the composite samples. Meanwhile, X-ray Diffractometry (XRD) was practiced for determation of the atomic and molecular structure of a crystal and UV-Vis spectroscopy is used to indicate the bond

transition of the sample. A standard three electrode electrochemical cell was used to carry out the electrochemical measurements in which a platinum wire act as auxiliary electrode, glassy carbon electrode (GCE) as working electrode and reference electrode of Ag/AgCl. The cyclic voltammetry was obtained in  $5\mu$ M K<sub>4</sub>[Fe(CN)<sub>6</sub>] and 1 M KCl at different scan rates in the potential range of -0.2 to 0.8 V at room temperature.

#### Fabrication of Au-PEDOT/rGO/GCE

Before the surface modification of the bare glassy carbon electrode (3 mm in diameter), the surface was polished with fine alumina slurry (0.05  $\mu$ m) and rinse thoroughly with deionized water. The GCE was then ultra-sonicated in the acetone and deionized water successively and dry under ambient condition. The Au-PEDOT/rGO (1.0 mg) was added into 1 mL of deionized water and produced a homogeneous suspension after completion of one-hour sonication. Finally, 5  $\mu$ L of the Au-PEDOT/rGO homogenized solution was drop-casted on the pretreated GCE and allowed to dry in a vacuum desiccator for 2 hours.

#### **Determination of UA**

0.05 M of phosphate buffer solution (PBS saline) was prepared by mixing the two substance of 8.41 g of potassium dihydrogen phosphate (KH<sub>2</sub>PO<sub>4</sub>) and 6.63 g of di-potassium hydrogen phosphate (K<sub>2</sub>HPO<sub>4</sub>). The UA standard solution was then prepared by dissolving the UA standard powder with the PBS saline prepared previously. Then, differential pulse voltammetry (DPV) technique was practiced to obtain the oxidation peak of the UA (concentration ranging from 0.1  $\mu$ M to 25.0  $\mu$ M) through voltammograms. The voltammogram analysis were then used to plot a calibration curve, and the analysis was used as an indicator to determine the lowest detection of UA.

#### **Results and Discussion**

#### FTIR and XRD analyses

Figure 1 shows the FTIR spectra of graphite powder, GO, rGO, Au/rGO, and Au-PEDOT/rGO. From the figure, no significant peaks are observed for raw graphite. However, the GO spectrum showed a peak at 1051cm<sup>-1</sup>, which is attributed to the C-O bond, indicating that GO was successfully oxidized by the

graphite. The peak at 1620 cm<sup>-1</sup> was appointed to the alkene group C=C stretching and the 1724 cm<sup>-1</sup> indicated C=O stretching. A broad peak at 3392 cm<sup>-1</sup> indicated O-H stretching vibrations of C-OH groups. As expected, rGO bands are relatively weaker as it was reduced from GO to rGO by hydrazine hydrate. The intensities of oxygen-containing functional group absorption bands such as C-O at 1564 cm<sup>-1</sup> and O-H stretchings at 3417 cm<sup>-1</sup> are dramatically reduced. Also found to have disappeared from the rGO composites were the C=O and C=C stretchings. This shows that after the reduction process, rGO was successfully obtained.

Accordingly, the intent for the reduction of GO was to remove the epoxy and hydroxyl groups on the spectra, while other functional groups such as carbonyl, carboxyl and ester groups present on the edges of the carbon plane do not interfere with the conductivity of the rGO sheet. For the FTIR spectrum of Au/rGO, the peak present at 3466 cm<sup>-1</sup> is linked to the stretching of O-H. The 1575 cm<sup>-1</sup> absorption peak represents epoxide C-O vibration. There are no additional Au peaks detected, but due to Au doping on rGO, the intensity is increased. Therefore, the spectrum of Au/rGO should correspond to rGO composite. However, for the FTIR spectrum of Au-PEDOT/rGO, the vibrational band at 1512 cm<sup>-1</sup> was due to the formation of C=C and the absorption peak at 1346 cm<sup>-1</sup> is assigned to the C-C stretching in the ethylene dioxy group of the thiophene ring structure [20]. The C-S bond in the thiophene ring appeared at the wavenumber of 975 cm<sup>-1</sup> and 840 cm<sup>-1</sup>.

The XRD patterns for GO, rGO, Au/rGO, and Au-PEDOT/rGO are illustrated in Figure 2. The diffractogram of characteristic peak of GO was observed at  $10.25^{\circ}$  that represents a wider interlayer distance between the GO layers. This is the result of the oxidation of graphite during the synthesis process and also due to the formation of certain functional groups such as epoxy, carboxyl and hydroxyl which is supported in the FTIR results [21]. Meanwhile, the XRD pattern of rGO showed a broad diffraction peak at  $2\theta = 23.0^{\circ}$  due to the removal of oxygen functional group from GO which indicated that the rGO was successfully obtained. According to the XRD pattern of Au/rGO composites,

diffraction peaks at  $2\theta = 38.2^{\circ}$ ,  $44.45^{\circ}$ ,  $65.61^{\circ}$ ,  $77.61^{\circ}$ , and  $82.61^{\circ}$  are indexed to the (111), (200), (220), (311), and (222) planes of well crystalline Au with cubic phase. The diffraction peak corresponds to 002 from rGO layers and is complimented by a broad graphitic peak that appears at  $2\theta = 23^{\circ}$ . The diffractogram of AuNP-PEDOT/rGO showed similar pattern and diffraction peaks with Au/rGO showed more intense  $2\theta$  peak. The  $2\theta$  peak appeared at  $38.05^{\circ}$ ,  $44.17^{\circ}$ ,  $64.52^{\circ}$ ,  $77.30^{\circ}$  and  $81.84^{\circ}$ , which corresponded to the reflection planes of Au (111), Au (200), Au (220), Au (311) and Au (222), respectively. Furthermore, a broad diffraction peak at  $23.0^{\circ}$  belonging to C (002) from PEDOT and rGO was also observed [22]. This proved that metallic gold appeared in AuNPs/PEDOT/rGO sheets.

#### **SEM** analysis

SEM was utilized to observe the morphology of graphite, GO, rGO, Au/rGO, and Au-PEDOT/rGO. It provided a highly magnified image of the composite surface. Figure 3a shows the image of graphite (at

5000X magnification) which is as platelet-like crystalline form of carbon. It could be clearly seen that graphite was arranged and presented as a typical multilayer structure in agglomerates. However, GO (Figure 3b) showed the wrinkled aggregates composite with multiple folds which is related to the oxidation process to promote oxygen-containing functional groups on the graphite sheets. The formation of rGO (Figure 3c) produced more rough wrinkles compared to GO. This is due to the reduction process by hydrazine hydrate. In Figure 3d, Au particles were uniformly distributed across the rGO. As compared to the rGO micrograph, the Au nanoparticles were seen to be successfully incorporated and covered the rGO surface. Meanwhile, the bubble-like shape (Figure 3e) indicates that the Au/PEDOT particle displayed an irregular shape and uniformly wrapped the rGO sheet. The wrinkled sheet of rGO provided an attachment site for Au along with PEDOT particle [23].

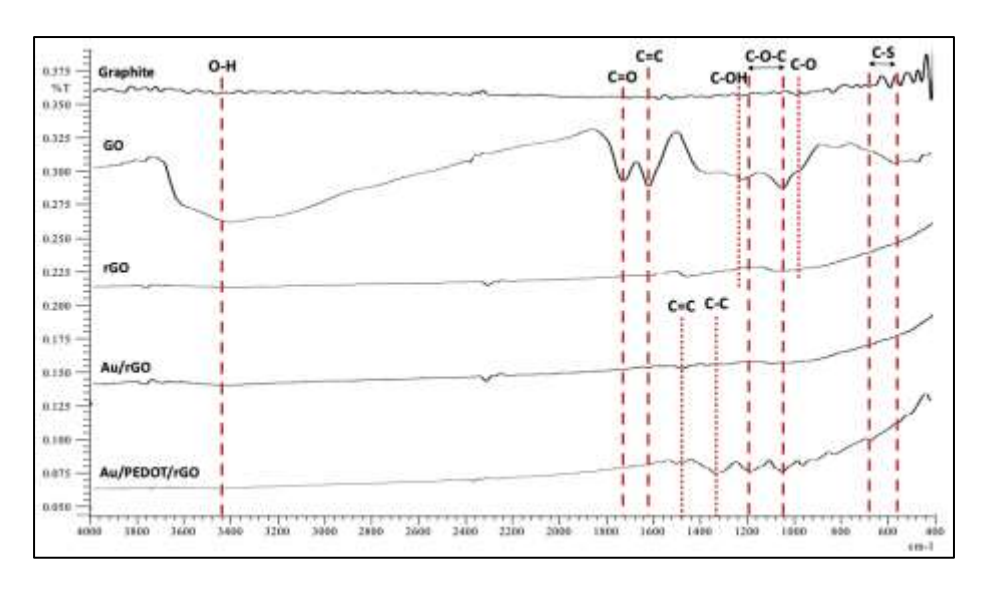


Figure 1. FTIR spectra measured of graphite, GO, rGO, Au/rGO and Au-PEDOT/rGO electrocatalyst

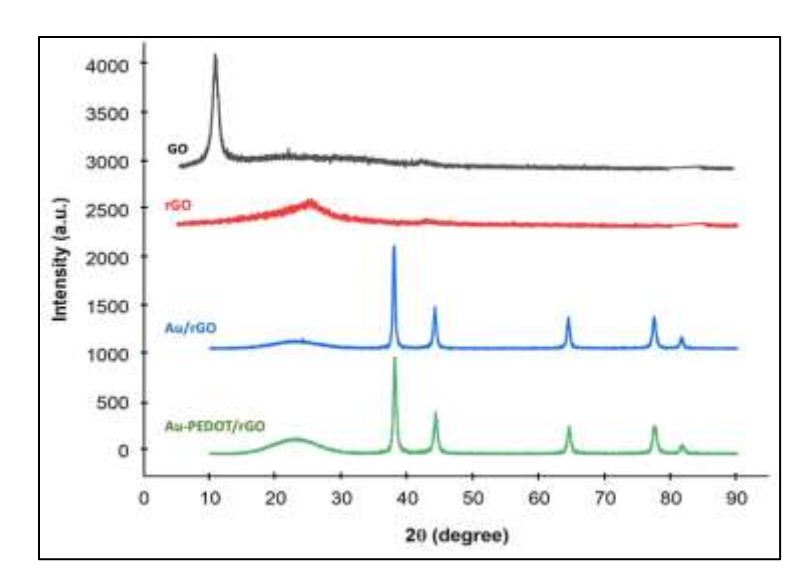


Figure 2. XRD pattern of GO, rGO, Au/rGO and Au-PEDOT/rGO

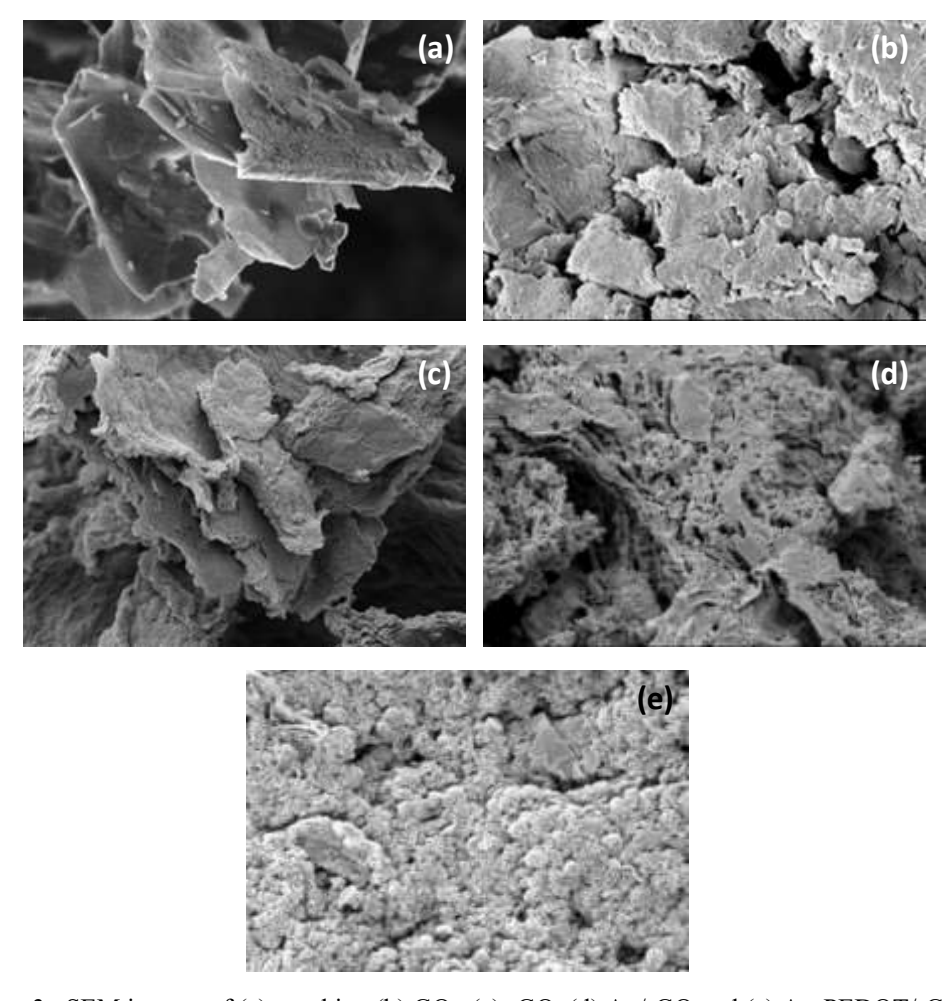


Figure 3. SEM images of (a) graphite, (b) GO, (c) rGO, (d) Au/rGO and (e) Au-PEDOT/rG

#### **UV-Vis analysis**

Figure 4 shows the UV-visible spectra of rGO, Au/rGO, and Au-PEDOT/rGO while Figure 4: Inset shows the comparison of UV spectrum of all composites with the presense of GO. The UV-visible spectrum of GO had the highest absorption peak at 228 nm indicating the  $\pi$ - $\pi$ \* transition C=C aromatic bonds [24]. As for rGO, the absorption peak had been reduced which proves the reduction process of rGO by hydrazine hydrate. Au/rGO had absorption peaks at 268 nm and 525 nm, while Au-PEDOT/rGO showed an absorption peaks of 226 nm and 510 nm. The formation of gold nanoparticles decorated on the rGO surface was demonstrated by the broad absorption peak observed for Au/rGO and Au-PEDOT/rGO at 510 nm and 525 nm, respectively, due to the active surface plasmon resonance of Au particle. The lowest absorbance represents the simultaneous reduction of Au<sup>3+</sup> to Au as well as reduction of GO to rGO resulting in Au/rGO and Au-PEDOT/rGO.

#### **Electrochemical characterization**

A cyclic voltammetry technique exploiting the solution based redox probe [Fe(CN)<sub>6</sub>]<sup>4</sup> was used to analyze the electrochemical features of the modified electrode as shown in Figure 5a. In theory, the CVs of all four modified electrodes (GO/GCE, rGO/GCE, Au/rGO/GCE, and Au-PEDOT/rGO/GCE) were expected to show higher in redox peak current and smaller peak separation compared to bare GCE. In these cases, Au-PEDOT/rGO showed the higher redox peak current than bare, GO, rGO and Au/rGO modified electrodes and enhanced electron transfer between the electrode surface and electrolyte that showed a high electron transfer of composite Au-PEDOT/rGO compared to other modified electrodes studied.

To further investigate the behaviour of Au-PEDOT/rGO modified electrode, the effect of current toward different scan rates was also examined (Figure 5b). From this figure, the oxidation peak current increased proportionally with scan rate. This finding can be explained by the limited electron transfer process of the system. The diffusion layer in a slow voltage scan rate will grow much farther from the electrode in comparison to a fast scan rate. Furthermore, the peak separation remaining at the same value shows a perfect reversibility

of electrode [12]. The result obtained also shows that the redox peak current increased linearly with the square root of scan rate (Figure 5c) indicating that redox reaction was controlled by the diffusion of [Fe(CN)6]<sup>-3/-4</sup> towards the electrode surface. According to the Randles-Sevcik formula (Equation 1), it can be clearly seen that the Ipa and Ipa increases against square roots of scan rate with a linear correlation coefficient of  $(r^2) = 0.9893$  and 0.9887, respectively where  $I_p$  is the oxidation peak current (A), n is the number of transferred electrons per mole, A is the active surface area of the electrode (cm<sup>2</sup>), D is the diffusion coefficient (cm<sup>2</sup>/sec), C is concentration (mol/cm<sup>3</sup>) and v is the scan rate (V/s). These results indicated that the redox reaction of [Fe(CN)6]-3/-4 on Au-PEDOT/rGO/GCE surface is a diffusion-controlled electrochemical processes.

$$I_{p} = (2.69 \times 10^{5}) n^{3/2} A D^{1/2} C v^{1/2}$$
 (1)

#### Electrochemical oxidation of UA at Au-PEDOT/rGO modified GCE

Electrochemical oxidation of 1 mM of UA was conducted on a bare GCE and Au-PEDOT/rGO modified GCE by CV to elucidate their electron transfer behavior in the presence of PBS (0.1 M) at a scan rate of 50 mVs<sup>-1</sup> and potential range in -0.2 V to 0.8 V (Figure 6). The Au-PEDOT/rGO/GCE demonstrated an immensely enhanced oxidation peak at potential of 0.45 V. In contrast, oxidation at the bare GCE showed a lower oxidation peak current at the same potential. It was obvious that Au-PEDOT/rGO/GCE produced highly enhanced catalytic current of UA oxidation compared to the bare GCE which can be attributed to the synergistic effect of the individual component in the nanocomposite, promoting the electron transfer between the redox probe and the electrode surface. This establishes that Au-PEDOT/rGO/GCE exhibit high electro-catalytic activity useful for UA detection. Figure 6 (inset) depicts a potential reaction for the oxidation of UA at the Au-PEDOT/rGO/GCE modified GCE. The oxidation of UA is a direct two-electron transfer mechanism where the 1H-purine-2,6,8 (9H)trione was converted by 1H-purine-2,6,8 (3H,7H,9H)trione which is also known as uric acid.

#### **Determination of UA by DPV**

DPV has much higher current sensitivity than the CV and therefore, lower UA concentrations can be analysed more accurately. The concentrations of UA ranging from 0.1  $\mu$ M to 25.0  $\mu$ M at the Au-PEDOT/rGO /GCE modified electrode in 0.1 M PBS solution are shown in Figure 7a. It was observed that the peak current increased with the increase in concentration. Figure 7b represents a linear calibration plot between peak current and concentration for the uric acid in the given range and gave the linear regression equation of  $y = 0.8915x + 10^{-1}$ 

2.647, with an  $r^2$  value of 0.9974. The limit of detection (LOD) for UA sample by using Au-PEDOT/rGO/GCE was calculated to be 0.05  $\mu M$  while the limit of quantification (LOQ) was determined to be 0.22  $\mu M$ . The synergistic effect of Au-PEDOT and rGO for the sensitive detection of UA could be contributed to the outstanding electrocatalytic performance. For UA detection, this potential modified electrode was compared to other similar electrodes, as shown in Table 1.

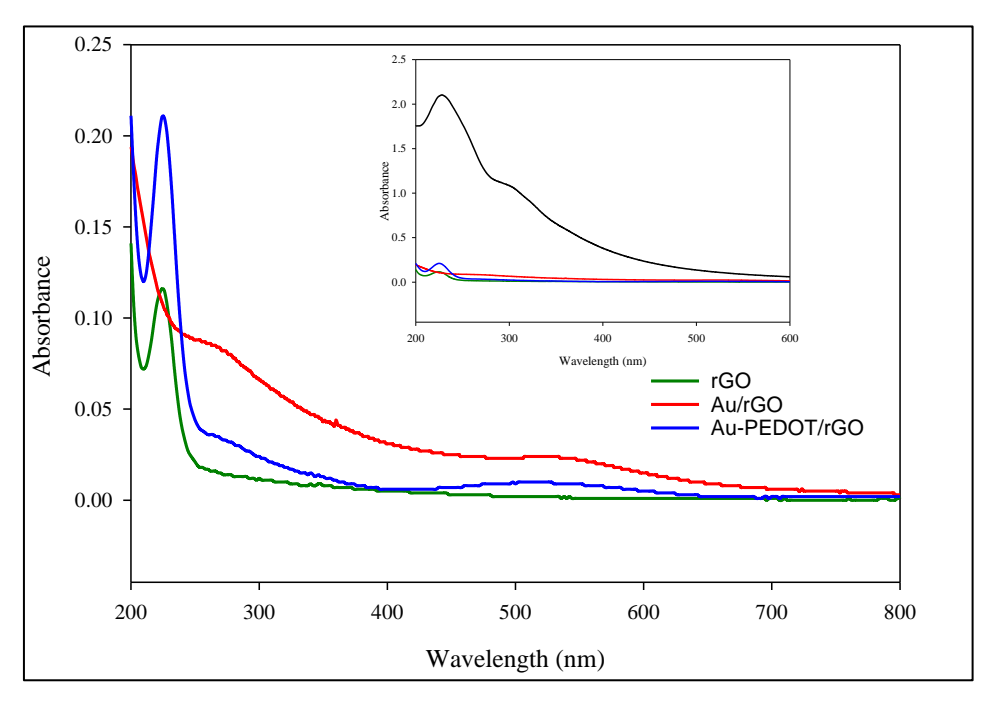


Figure 4. UV spectra of rGO, Au/rGO and Au-PEDOT/rGO. Inset: Comparison of UV spectra of all composites with the presence of GO (black line)

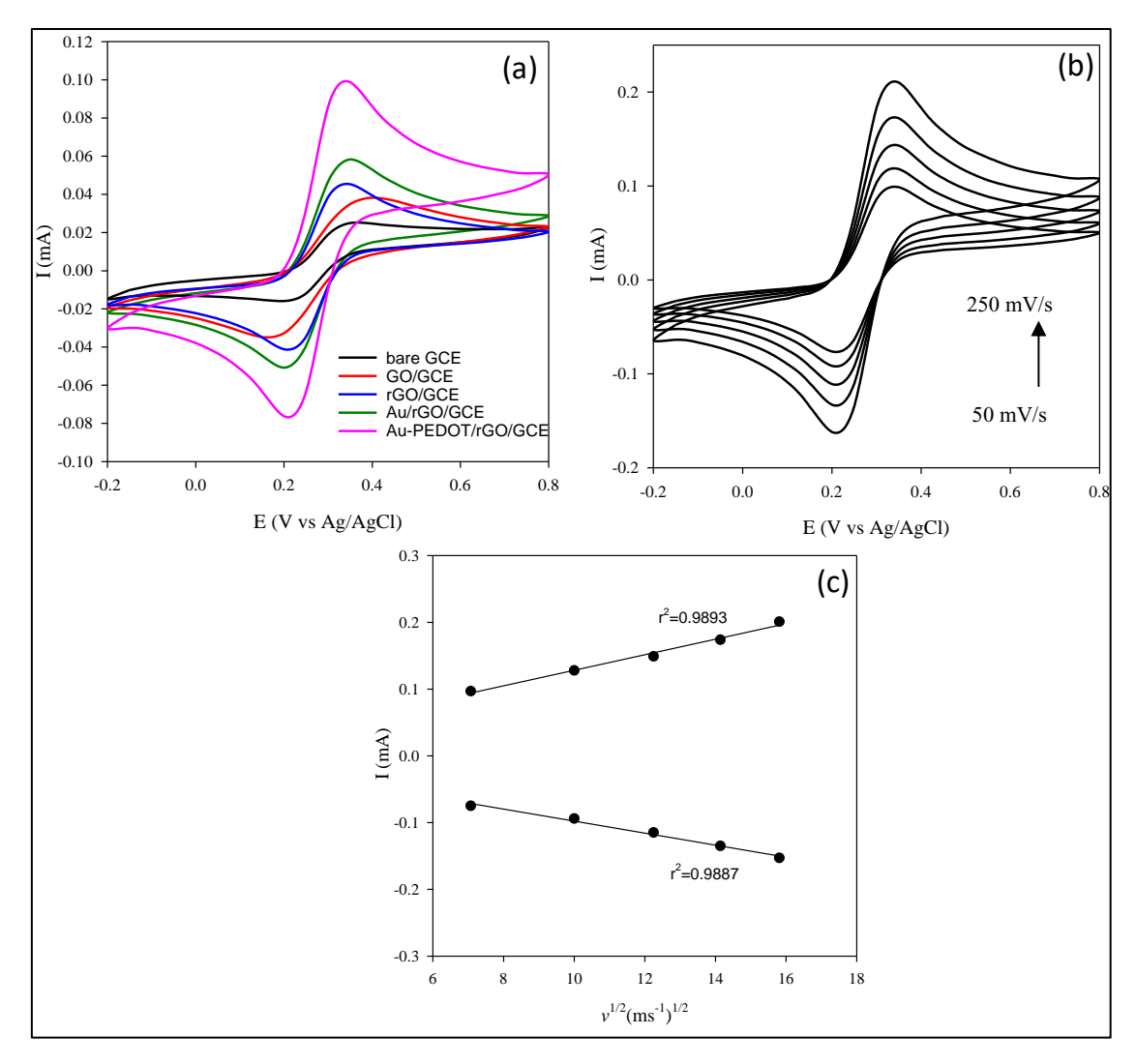


Figure 5. (a) Cyclic voltammogram of modified electrode in  $5\mu M$  K<sub>4</sub>[Fe(CN)<sub>6</sub>] and 1 M KCl electrolyte solution with scan rate of 100 mV/s, (b) Cyclic voltammograms of Au-PEDOT/rGO/GCE at different scan rate in  $5\mu M$  K<sub>4</sub>[Fe(CN)<sub>6</sub>] and 1 M KCl electrolyte solution and (c) The plot of square root of scan rate vs. current

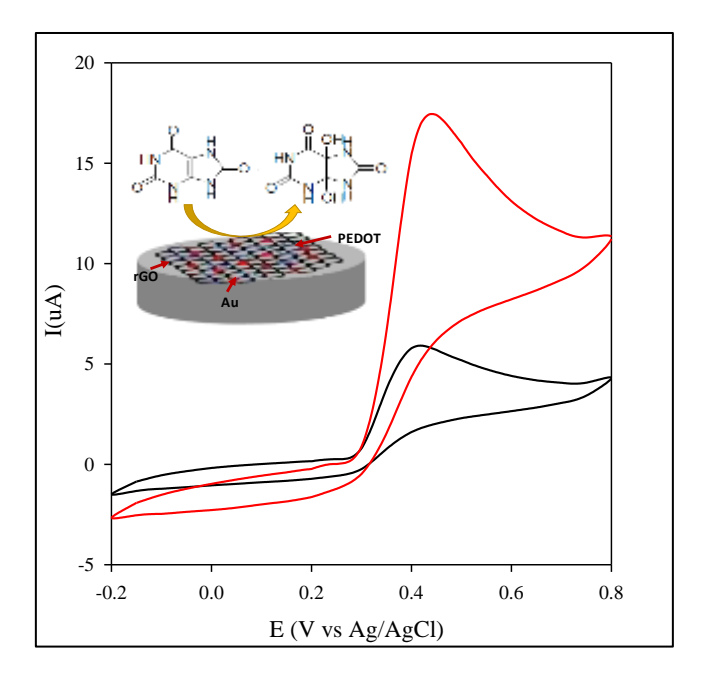


Figure 6. (a) Cyclic voltammograms obtained at the bare GCE (black line) and Au-PEDOT/rGO/GCE (red line) in 0.1 M of PBS (pH 7) containing 1.0 mM of UA. Inset: Electrocatalytic oxidation of UA at Au-PEDOT/rGO/GCE

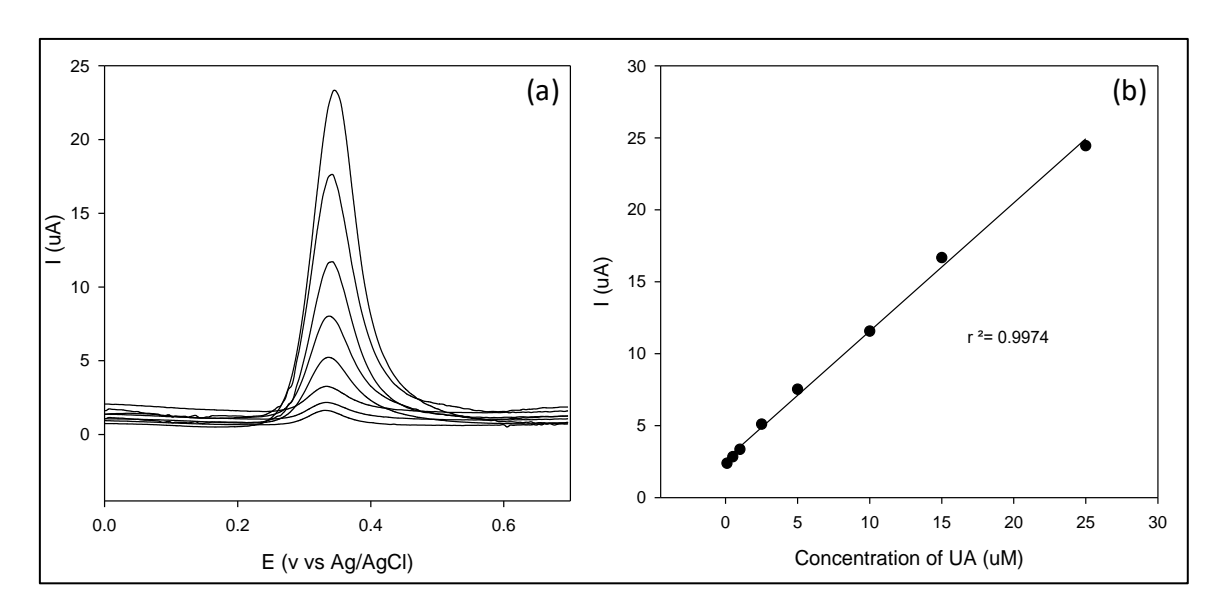


Figure 7. (a) DPV response measured over a range of UA concentration from 0.1  $\mu M$  to 25.0  $\mu M$  and (b) The relationship between the oxidation peaks current against UA concentration

Modified electrode	<b>Type of Detection</b>	Linear Range	Limit of Detection (µM)	Ref
PEDOT/Au	DPV	2.0-600 μΜ	1.50	[25]
Au/rGO/GCE	DPV	6.8-41 μM	1.40	[26]
Au/rGO	SWV	0.5-60 μΜ	0.21	[27]
3D Electrochemically rGO	DPV	0.1-10 μΜ	0.10	[28]
PEDOT/Au hollow nanosphere	DPV	0.15-330 μΜ	0.08	[22]
Au nanocoral/PET	Amperometry	0.2-600 μΜ	0.06	[29]
Au-PEDOT/rGO/GCE	DPV	0.1-25.0 μΜ	0.05	This work

Table 1. Comparison of various type of modified electrode for detection of uric acid in human urine sample

#### Conclusion

In summary, Au-PEDOT/rGO modified electrode has been synthesized by a facile method. The product was characterized by FTIR that observed C-O-C and C-S stretching indicates the PEDOT has successfully presenced in the composite. The morphology of Au-PEDOT/rGO by SEM shows the Au along with PEDOT has attached to rGO sheets. Glassy carbon electrode was modified with Au-PEDOT/rGO and underwent electrochemical characterization by using CV for the detection of UA and shows excellent electrical properties. The detection limit of UA by Au-PEDOT/rGO/GCE in PBS solution is calculated to be 0.05 µM over a linear range of 0.1 µM to 25.0 µM via a DPV studies. The results suggested the great potential use of Au-PEDOT/rGO in selectively non-enzymatic sensing of UA.

#### Acknowledgments

The authors are grateful to Research Acculturation Grant Scheme (RAGS) RAGS/1/2015/ST0/UMT/03/ for financial support as well as Universiti Malaysia Terengganu for providing facilities for undertaking this research.

#### References

1. Yu, H., Zhang, Z., Shen, T., Jiang, J., Chang, D. and Pan, H. (2018). Sensitive determination of uric acid by using graphene quantum dots as a new substrate for immobilisation of uric oxidase. *IET Nanobiotechnology*, 12(23): 191-195.

- Soares, F., Paula, F. D. S., Franco, D. L., Torres, W. and Ferreira, L. F. (2017). Electrochemical detection of uric acid using graphite screen-printed electrodes modified with prussian blue/poly(4-aminosalicylic acid)/uricase. *Journal of Electroanalytical Chemistry*, 806: 172-179.
- 3. Ndrepepa, G. (2018) Uric acid and cardiovascular disease. *Clinica Chimica Acta*, 484(3): 150-163.
- Black, C. N., Bot, M., Peter, G., Snieder, H. and Penninxm B. W. J. H. (2017). Uric acid in major depressive and anxiety disorders. *Journal of Affective Disorders*, 225: 684-690.
- Kand, R., Drábková, P. and Hampl, R. (2011). The determination of ascorbic acid and uric acid in human seminal plasma using an HPLC with UV detection. *Journal of Chromatography B*, 879: 2834-2839.
- Long, Q., Fang, A., Wen, Y., Li, H., Zhang, Y. and Yao, S. (2016). Biosensors and bioelectronic rapid and highly-sensitive uric acid sensing based on enzymatic catalysis-induced upconversion inner filter effect. *Biosensors and Bioelectronic*, 86: 109-114.
- 7. Wei, Y., Liu, Y., Xiu, Z., Wang, S., Chen, B., Zhang, D. and Fang, Y. (2020). Simultaneous detection of ascorbic acid, dopamine, and uric acid using a novel electrochemical sensor based on palladium nanoparticles/reduced graphene oxide nanocomposite. *International Journal of Analytical Chemistry*, 1-13.

- 8. Su, C. H., Sun, C. L. and Liao, Y. L. (2017). Printed combinatorial sensors for simultaneous detection of ascorbic acid, uric acid, dopamine and nitrite. *ACS Omega*, 2(8): 4245-4252.
- 9. Tukimin, N., Abdullah, J. and Sulaiman, Y. (2018). Electrodeposition of poly(3,4-ethylenedioxy thiophene)/reduced graphene oxide/manganese dioxide for simultaneous detection od uric acid, dopamine and ascorbic acid. *Journal of Electroanalytical Chemistry*, 820: 74-81.
- Muhamad, N. B., Khairul, W. M. and Yusoff, F. (2019). Synthesis and characterization of poly(3,4-ethylenedioxythiophene) functionalized graphene with gold nanoparticles as a potential oxygen reduction electrocatalyts. *Journal of Solid State Chemistry*, 275(4): 30-37.
- 11. Li, Y., Du, Y., Dou, Y., Cai, K. and Xu, J. (2017). PEDOT-based thermoelectric nanocomposites- a mini review. *Synthetic Metals*, 226: 119-128.
- 12. Lawal, A. T. (2019). Graphene-based nano composites and their applications. A review. *Biosensors and Bioelectronics*, 2019: 111384.
- 13. Rosli, A. R., Loh, S. H. and Yusoff, F. (2019). Synthesis and characterization of magnetic fe<sub>3</sub>0<sub>4</sub>/reduced graphene oxide and its application in determination of dopamine. *Asian Journal of Chemistry*, 31(12): 2785-2792.
- 14. Berisha, L., Shabani, E., Maloku, A., Jashari, G. and Arbneshi, T. (2020). Electrochemical determination of dopamine and uric acid in blood serum using anionic surfactants at carbon paste electrodes. *Malaysian Journal of Analytical Sciences*, 24(1): 97-106.
- Jin W. and Maduraiveeran, G. (2017).
   Electrochemical detection of chemical pollutants based on gold nanomaterials. *Trends in Environmental Analytical Chemistry*, 14(4): 28-36.
- 16. Harun, N. A., Kassim, S., Tahrin, R. A. A. and Rusdi, N. F. (2018). Bimetallic (Au-Ag) in 3D hot spots as highly sensitive substrate for high performance surface-enhanced raman scattering (SERS). *ASM Science Journal*, 11(1): 86-95.
- 17. Kassim, S., Padmanabhan, S. C., Salaun, M. and Pemble, M. E. (2011). PMMA gold metallodielectric photonic crystals and inverse opals: preparation and optical properties. *AIP*

- Conference Proceeding, 263: 1-4.
- 18. Kaur, M., Kaur, H., and Kukkar, D. (2018). Synthesis and characterization of graphene oxide using modified Hummer's method. *AIP Conference Proceeding*, 1953(1): 030180.
- Johra, F. T. and Jung, W. (2016). Low temperature synthesis of RGO-Au nanocomposite for apparently reduced time and its application as a chemical sensor. *Applied Surface Science*, 362: 169-175.
- Liu, Z., Xu, J., Yue, R., Yang, T. and Gao, L. (2016). Facile one-pot synthesis of Au-PEDOT/rGO nanocomposite for highly sensitive detection of caffeic acid in red wine sample. *Electrochimica Acta*, 196: 1-12.
- 21. Yan, Q., Zhi, N., Yang, L., Xu, G., Feng, Q., Zhang, Q. and Sun, S. (2020). A highly sensitive uric acid electrochemical biosensor based on a nano-cube cuprous oxide/ferrocene/uricase modified glassy carbon electrode. *Scientific Reports*, 10: 10607.
- 22. Ali, A., Zhang, Y., Jamal, R., and Abdiryim, T. (2017). Solid-state heating synthesis of poly(3,4-ethlylenedioxythiophene)/gold/graphene composite and its application for amperometric determination of nitrite and iodate. *Nanoscale Research Letter*, 12(568): 1-10.
- 23. Muhammad, N. B., and Yusoff, F. (2018). The physical and electrochemical characteristic of gold nanoparticles supported PEDOT/graphene composite as potential cathode material in fuel cells. *Malaysian Journal of Analytical Sciences*, 22(6): 921–930.
- 24. Gualandi, I., Tonelli, D., Mariani, F., Scavetta, E., Marzocchi, M. and Fraboni, B. (2016). Selective detection of dopamine with an all PEDOT:PSS organic electrochemical transistor. *Scientific Reports*, 6 (10): 1-10.
- Sekli-belaidi, F., Temple-boyer, P. and Gros, P. (2010). Voltammetric microsensor using PEDOT-modified gold electrode for the simultaneous assay of ascorbic and uric acids. *Journal of Electroanalytical Chemistry*, 647(2): 159-168.

- 26. Wang, C., Du, J. and Wang, H. (2014). A facile electrochemical sensor based on reduced graphene oxide and Au nanoplates modified glassy carbon electrode for simultaneous detection of ascrobic acid, dopamine and uric acid. *Sensors & Actuators: B. Chemical*, 204: 302-309.
- Tian, X., Cheng, C. and Yuan H. (2012).
   Simultaneous determination of L-ascorbic acid, dopamine and uric acid with gold nanoparticles—β-cyclodextrin—graphene-modified electrode by
- square wave voltammetry. Talanta, 93: 79-85.
- 28. Yu, X., Sheng, K. and Shi, G. (2014). A Three-dimensional interpenetrating electrode of reduced graphene oxide for selective detection of dopamine. *The Analyts*, 139: 4525-4531.
- 29. Hsu, M., Chen, Y., Lee, C., and Chiu, H. (2012). Gold nanostructures on flexible substrates as electrochemical dopamine sensors. *Applied Material and Interface*, 4(10): 5570-5575.

## Malaysian Journal of Analytical Sciences (MJAS) Published by Malaysian Analytical Sciences Society

#### SITE-SELECTIVE CARBOXYMETHYLATION OF CHITOSAN UNDER HETEROGENEOUS CONDITIONS

(Penentuan Tapak bagi Proses Pengkarboksimetil pada Kitosan dalam Keadaan Heterogen)

Nur Ellina Annisa Salehuddin<sup>1</sup>, Nurul Adilah Rodzali<sup>1</sup>, Ku Halim Ku Bulat<sup>2</sup>, Nadhratun Naiim Mobarak<sup>1\*</sup>

<sup>1</sup> Department of Chemical Sciences, Faculty of Science and Technology Universiti Kebangsaan Malaysia, 43600 Bangi, Selangor, Malaysia <sup>2</sup>School of Fundamental Science Universiti Malaysia Terengganu, 21030 Kuala Nerus, Terengganu, Malaysia

\*Corresponding author: nadhratunnaiim@ukm.edu.my

Received: 11 March 2021; Accepted: 22 May 2021; Published: 27 June 2021

#### Abstract

The substitution sites on chitosan are affected by the presence of a base. Herein, the effects of pH on the site-selective carboxymethylation of chitosan were investigated. Carboxymethyl chitosan was synthesized by reacting chitosan with monochloroacetic acid at different pH under heterogeneous conditions. Fourier transform infrared-attenuated total reflectance (FTIR-ATR) spectroscopy confirmed that carboxymethylation was successful, with the appearance of peaks around 1326-1320 cm<sup>-1</sup> (C–N groups) and 1257-1253 cm<sup>-1</sup> (C–O–C groups) and allowed differentiation between the carboxymethyl substitution sites on chitosan. Additionally, the peaks at approximately 3.28 and 4.12 ppm in the <sup>1</sup>H nuclear magnetic resonance (NMR) spectra confirmed that substitution occurred at amine and hydroxyl groups, respectively. Overall, the carboxymethylation of chitosan under heterogeneous conditions at pH 8.5-11 gave O-substitution, at pH 12-13 gave N,O-substitution, and at pH 14 gave N-substitution. This pH dependence of the site-selective substitution of chitosan is important for polymer electrolyte application.

Keywords: carboxymethyl chitosan, pH effect, substitution site, heterogeneous conditions

#### **Abstrak**

Tapak penggantian kitosan dipengaruhi oleh kehadiran bes. Dalam kajian ini, kesan pH terhadap tapak penggantian pengkarboksimetil kitosan telah dikaji. Karboksimetil kitosan disintesis melalui tindak balas kitosan dengan asid monokloroasetik pada pH berbeza dalam keadaan heterogen. Spektroskopi inframerah transformasi Fourier (ATR-FTIR) mengesahkan bahawa karboksimetilasi telah berjaya dilakukan dengan kemunculan puncak sekitar 1326-1320 cm<sup>-1</sup> (kumpulan C-N) dan 1257-1253 cm<sup>-1</sup> (kumpulan C-O-C), yang menunjukkan perbezaan tapak penggantian karboksimetil pada kitosan. Selain itu, puncak sekitar 3.28 dan 4.12 ppm dalam spektrum resonans magnetik nukleus (<sup>1</sup>H NMR) mengesahkan bahawa penggantian berlaku pada kumpulan amina dan hidroksil. Secara keseluruhan, karboksimetilasi kitosan dalam keadaan heterogen pada pH 8.5-11 memberikan penggantian pada tapak O, pH 12-13 memberikan penggantian pada tapak N dan O, dan pH 14 memberikan penggantian pada tapak N. Kebergantungan tapak pemilihan untuk penggantian kitosan dengan pH ini adalah penting untuk aplikasi elektrolit polimer.

Kata kunci: karboksimetil kitosan, kesan pH, tapak penggantian, keadaan heterogen

#### Introduction

Chitosan has been widely studied for various applications in the biomedical field owing to its biocompatible, biodegradable, nontoxic, and antimicrobial properties [1]. However, the limited solubility of chitosan in water and other organic solvents has restricted its potential in drug delivery and tissue engineering [2]. As a water-soluble derivative of chitosan, carboxymethyl chitosan (CM-chitosan) has better biological and physicochemical properties [3]. Furthermore, CM-chitosan is easy to synthesize and can be used for many applications in cosmetic, biomedical, environmental, food industry, and polymer electrolyte systems [4].

Several researchers have claimed that substitution occurs preferentially at the hydroxyl group at C6 in the chitosan structure rather than at the hydroxyl group at C3 and the amine group [4]. This selectivity is influenced by the steric hindrance at the hydroxyl group at C3 and the amine group. However, the choice of the appropriate reaction conditions and reagents allows the preparation of CM-chitosan derivatives with site-selective substitution at either the primary hydroxyl or amine group of chitosan to produce O-carboxymethyl chitosan (O-CM-chitosan), N-carboxymethyl chitosan (N-CM-chitosan), N,O-carboxymethyl chitosan (N,O-CM-chitosan), or N,N-carboxymethyl chitosan (N,N-CM-chitosan), as shown in Figure 1 [3-5].

The selection of a particular substitution site is important, as it influences the performance of chitosan derivatives for specific applications. According to a previous study, O-CM-chitosan has a higher moisture retention—absorption ability than N-CM-chitosan [6]. High moisture retention-absorption properties are crucial for applications in cosmetics, such as moisturizing skincare [7]. In contrast, low moisture retention—absorption properties are important for applications such as battery membranes [8].

O-CM-chitosan can be synthesized through direct alkylation by reacting chitosan, sodium hydroxide (NaOH), and monochloroacetic acid (ClCH<sub>2</sub>COOH) at different temperatures and reactant ratios under

heterogeneous conditions [9, 10]. Meanwhile, N-CMchitosan can be obtained through a reductive Nalkylation reaction [11]. The N-alkylation of chitosan can be carried out in the presence of various bases. The pK<sub>a</sub> of the reaction condition should be higher than 6.3 [12]. Previously, N-CM-chitosan and N,N-CM-chitosan have been prepared at pH 8 and pH 8.5, respectively. These reactions were carried out under homogeneous conditions and the pH was adjusted to 8 or 8.5 after the addition of ClCH2COOH [13, 14]. Other than these Nalkylation reactions, a prior study reported the unsuccessful preparation of N-octylchitosan under heterogeneous conditions, likely due to the high steric hindrance caused by using chitosan with a degree of deacetylation (DD) lower than 90% [15]. To the best of our knowledge, there have been no reports on the successful synthesis of N-CM-chitosan under heterogeneous conditions.

Therefore, in the present study, the effect of pH under heterogeneous conditions for the synthesis of N-CM-chitosan have been investigated. We also discussed the effect of pH on the degree of substitution (DS), as research has shown that the DS is influenced by the reaction conditions, with low DS values obtained for heterogeneous reactions and high DS values for homogeneous conditions [16]. We used Fourier transform infrared-attenuated total reflectance (FTIR-ATR) spectroscopy, <sup>1</sup>H nuclear magnetic resonance spectroscopy (NMR), and the DS to characterize and analyze the synthesized CM-chitosan derivatives. Computational modeling was also performed to understand the charges in all the structures.

#### **Materials and Methods**

#### Materials

Chitosan (DD = 89%, as calculated by <sup>1</sup>H NMR spectroscopy) was commercially obtained from ChitoChem. NaOH and ClCH<sub>2</sub>COOH were purchased from Sigma-Aldrich. Isopropanol (IPA), ethanol (EtOH), and acetic acid (CH<sub>3</sub>COOH) were purchased from Systerm. All materials were used without further purification.

#### Preparation of CM-chitosan derivatives

The carboxymethylation of chitosan was carried out based on previously reported work with minor modifications [17]. Briefly, 5 g of chitosan was suspended in 25 mL of IPA in a flask. Then, a mixture of 5 g of NaOH in 25 mL of water was added to the flask. The resulting mixture was stirred with a magnetic stirrer at 50 °C for 1 hour on a hot plate. The pH of the mixture (pH 8.5-14) was adjusted by adding NaOH dropwise using a micropipette. Subsequently, 7.5 g of ClCH<sub>2</sub>COOH dissolved in 25 mL of IPA was added to the reaction mixture. After stirring for 4 hours at 50 °C, the reaction was terminated by adding 70% EtOH (100 mL). The precipitate was filtered and rinsed with 70%, 80%, and 90% EtOH to obtain the final product. The final product, which was obtained as the Na-salt of CMchitosan, was stored in a desiccator for 3-5 days. The obtained products were denoted as CM-chitosan-8.5 (pH 8.5), CM-chitosan-9 (pH 9), CM-chitosan-10 (pH 10), CM-chitosan-11 (pH 11), CM-chitosan-12 (pH 12), CM-chitosan-13 (pH 13), and CM-chitosan-14 (pH 14). The masses of the obtained products were 7.8375 g (CM-chitosan-8.5), 7.0290 g (CM-chitosan-9), 6.2343 g (CM-chitosan-10), 6.4860 g (CM-chitosan-11), 6.1240 g (CM-chitosan-12), 6.2510 g (CM-chitosan-13), and 6.562 g (CM-chitosan-14).

#### FTIR-ATR spectroscopy

FTIR-ATR spectra were recorded using a PerkinElmer Spectrum 2000 spectrometer in the range of 4000–650 cm<sup>-1</sup> with a scanning resolution of 2 cm<sup>-1</sup>. The FTIR-ATR analysis was conducted to observe the changes in the functional groups before and after chitosan modification.

#### <sup>1</sup>H NMR spectroscopy

NMR analysis was performed to confirm the N- and O-substitution of the CM-chitosan derivatives.  $^{1}H$  NMR spectra were recorded using a Bruker Avance 111 spectrometer (400 MHz). Chitosan and the CM-chitosan derivatives were dissolved in a mixture of 1% CD<sub>3</sub>COOD in D<sub>2</sub>O [18].

#### DS of CM-chitosan derivatives

To determine the DS of each CM-chitosan derivatives, the Na form was changed to the H-form [19, 20]. First,

1.5 g of Na-form CM-chitosan was suspended in 80% EtOH (100 mL) and then 37% hydrochloric acid (10 mL) was added. After stirring the mixture was with a magnetic stirrer for 30 min, the precipitate was filtered and rinsed with 70–90% EtOH. The products were stored in a desiccator for 2–3 days.

The DS represents the average number of substitutions per anhydroglucose unit (AGU). The DS values of the CM-chitosan derivatives were determined by the standard ASTM D1439 method, as previously reported [21]. First, 0.5 g of dry H-form CM-chitosan was dispersed in 100 mL of distilled water in a flask. Then, 25 mL of NaOH solution (0.3 M) was added to the suspension and the resulting mixture was stirred for 15 min at 40 °C. Three drops of phenolphthalein were then added to the mixture as an indicator. Finally, the mixture was titrated with 0.3 M HCl until the indicator changed from pink to colorless. A blank test also was carried out using the same procedure without adding a CM-chitosan derivative.

The percentage of CM groups (%CM) and the DS were calculated using equations (1) and (2), respectively.

$$\%CM = \frac{[(Vo - Vn)M \times 0.059 \times 100]}{m} \tag{1}$$

$$DS = \frac{162 \times \%CM}{[5900 - (58 \times \%CM)]} \tag{2}$$

where  $V_0$  is the volume of HCl used for the blank test (mL),  $V_n$  is the volume of HCl used for sample titration (mL), M is the molar concentration of HCl (M), m is the amount of sample (g), 162 is the molar mass of the AGU, and 59 is the molar mass of a CM group (– CH<sub>2</sub>COOH).

The differences between means were analyzed for statistical significance using Student's t-test. A value of p < 0.05 was considered significant [22].

#### **Computational modeling studies**

Density functional theory (DFT) calculations implemented in Gaussian 09 were used to investigate the Mulliken charge and stability of all the CM-chitosan structures. The GaussView 5.0 program was used for

molecular visualization. The gas-phase molecular structure of chitosan and all the CM-chitosan derivatives in the ground state were optimized by DFT in its restricted form without any symmetry constraint. To produce accurate ground state geometries, chitosan and the CM-chitosan derivatives were modeled using two monomers. The chitosan monomer consists of glucosamine and *N*-acetylglucosamine. For O-CM-

chitosan, the hydroxyl groups on the chitosan chain were substituted with CM groups (–CH<sub>2</sub>COOH). For N-CM-chitosan, the CM groups were substituted at the amine groups. For N,O-CM-chitosan, both the hydroxyl and amine groups were substituted with CM groups. All the structures were minimized using the B3LYP/6-31++G (d,p) basis set.

Figure 1. Structures of chitosan and CM-chitosan derivatives

### Results and Discussion Characterization by FTIR-ATR spectroscopy

CM-chitosan can be synthesized through a direct alkylation process. Figure 2 shows the FTIR-ATR spectra of chitosan and the various CM-chitosan derivatives. In the FTIR-ATR spectrum of chitosan, the peaks at 3283, 2868, 1644, 1585, and 1060 cm<sup>-1</sup>

represent O–H stretching, C–H stretching, the N–C(O)–CH<sub>3</sub> carbonyl, N–H bending, and C–O stretching, respectively. The positions of these peaks are similar to those reported in a previous study [23]. In contrast, in the FTIR-ATR spectra of all the CM-chitosan derivatives, a new peak appears around 2922–2954 cm<sup>-1</sup>, corresponding to the methylene of the CM group,

which confirmed the carboxymethylation of chitosan. Additional new peaks at 1648-1634 cm<sup>-1</sup> and 1588-1585 cm<sup>-1</sup> correspond to the N-acetyl and carboxylate of the CM group, respectively.

However, intense peaks around 1533-1529 cm<sup>-1</sup>, 1386-1379 cm<sup>-1</sup>, and 1257-1253 cm<sup>-1</sup> are only observed for CM-chitosan-8.5 to CM-chitosan-13. These peaks can be assigned to the amide II group, symmetrical -COO<sup>-</sup> stretching, and ether groups, respectively. In contrast, the intense peaks observed around 1326-1320 cm<sup>-1</sup> for CM-chitosan-12 and CM-chitosan-13 correspond to C-N stretching. In addition, CM-chitosan-14 exhibits peaks around 1414, 1376, and 1327 cm<sup>-1</sup>, representing symmetrical -COO stretching, the amide III group, and C-N stretching, respectively. These peaks have also been reported in a previous study [24]. As well as confirming that carboxymethylation occurred, these observations provided an initial indication that the CM groups had been substituted at hydroxyl groups for CMchitosan-8.5 to CM-chitosan-13 and at amine groups for CM-chitosan-12 to CM-chitosan-14. These findings were further confirmed by 1H NMR analysis and determination of the DS.

#### Characterization by <sup>1</sup>H NMR spectroscopy

Figure 3 shows the <sup>1</sup>H NMR spectra of chitosan and the CM-chitosan derivatives obtained under different pH conditions. The proton assignments for chitosan are as follows. <sup>1</sup>H NMR (400 MHz, 1% CD<sub>3</sub>COOD/D<sub>2</sub>O), δ (ppm): 2.17 (H7), 3.11 (H2), 3.66–3.84 (H3, H4, H5, H6), 4.81 (H1). The DD was calculated based on the intensity of the <sup>1</sup>H NMR peaks using Equation (3) [25].

$$DD(\%) = \left\{1 - \left(\frac{1}{3}I_{CH3} / \frac{1}{6}I_{H2-H6}\right)\right\} \times 100 \tag{3}$$

Following the substitution of CM groups, new peaks, assigned as H8a and H8b, should be observed. Furthermore, the H1 peak should appear at approximately 4.80 ppm as reported by previous study [26–28] but this peak was not apparent owing to overlap with the solvent signals.

The proton assignments for the CM-chitosan derivatives are as follows:

 $^{1}H$ NMR (400 CM-chitosan-8.5. MHz, 1% CD<sub>3</sub>COOD/D<sub>2</sub>O), δ (ppm): 2.18 (H7), 3.13 (H2), 3.67– 3.84 (H3, H4, H5, H6), 4.11 (H8a), 4.81 (H1). CMchitosan-9. <sup>1</sup>H NMR (400 MHz, 1% CD<sub>3</sub>COOD/D<sub>2</sub>O), δ (ppm): 2.17 (H7), 3.13 (H2), 3.67–3.85 (H3, H4, H5, H6), 4.12 (H8a), 4.81 (H1). CM-chitosan-10. <sup>1</sup>H NMR (400 MHz, 1% CD<sub>3</sub>COOD/D<sub>2</sub>O), δ (ppm): 2.17 (H7), 3.12 (H2), 3.67-3.87 (H3, H4, H5, H6), 4.12 (H8a), 4.81 (H1). CM-chitosan-11. <sup>1</sup>H NMR (400 MHz, 1% CD<sub>3</sub>COOD/D<sub>2</sub>O), δ (ppm): 2.17 (H7), 3.12 (H2), 3.67– 3.85 (H3, H4, H5, H6), 4.13 (H8a), 4.81 (H1). CMchitosan-12. <sup>1</sup>H NMR (400 MHz, 1% CD<sub>3</sub>COOD/D<sub>2</sub>O),  $\delta$  (ppm): 2.16 (H7), 3.11 (H2), 3.28 (H8b), 3.66–3.84 (H3, H4, H5, H6), 4.12 (H8a), 4.81 (H1). CM-chitosan-13. <sup>1</sup>H NMR (400 MHz, 1% CD<sub>3</sub>COOD/D<sub>2</sub>O), δ (ppm): 2.17 (H7), 3.12 (H2), 3.27 (H8b), 3.64-3.84 (H3, H4, H5, H6), 4.11 (H8a), 4.81 (H1). CM-chitosan-14. <sup>1</sup>H NMR (400 MHz, 1% CD<sub>3</sub>COOD/D<sub>2</sub>O), δ (ppm): 2.17 (H7), 3.11 (H2), 3.66–3.84 (H3, H4, H5, H6), 3.23 (H8b), 4.81 (H1).

Based on the <sup>1</sup>H NMR spectra in Figure 3, peaks at 4.11– 4.12 ppm are observed for CM-chitosan-8.5, CMchitosan-9, CM-chitosan-10, CM-chitosan-11, CMchitosan-12, and CM-chitosan-13. Furthermore, peaks at 3.23-3.28 ppm are observed for CM-chitosan-12, CM-chitosan-13, and CM-chitosan-14. The peaks in the region of 4.05-4.55 ppm correspond to protons of CM groups (-OCH2-COOD) substituted at the hydroxyl groups at the C3 and C6 positions, as described in the previous study [27, 28]. In contrast, the peaks in the region of 3.25 ppm correspond to the protons of N-CH<sub>2</sub>-COOH groups, which are confirmed by the previous study that reported the substitution of CM groups at the amine groups at around 3.2 ppm [26, 29]. These results indicate that O-CM-chitosan can be attained at pH 8.5-11, whereas pH 12-13 gives N,O-CM-chitosan, and N-CM-chitosan can only be obtained at pH 14.

#### DS of CM-chitosan derivatives

The DS indicates the number of substituent groups attached per monomeric unit. Because chitosan has two hydroxyl groups and one amine group, the maximum DS value is 3 [20,21]. As depicted in Table 1, the DS values are close to 1 for all the CM-chitosan derivatives. Based on the NMR spectra, at pH 8.5–11, substitution occurred

at the hydroxyl groups. However, as the pH increases in this range, the DS decreases. Thus, the deprotonated hydroxyl group is expected to play an important role in producing O-CM-chitosan, as shown in Scheme 1.

Although the NMR spectra showed that substitution occurred at both the amine and hydroxyl groups at pH 12 and 13, DS values of 2 were not observed under these conditions. The DS values of 0.80 and 0.66 at pH 12 and 13, respectively as reported in Table 1, indicates that

incomplete substitution occurred at both functional groups at these pH values. However, it is possible that the degree of substitution at each site differed depending on the pH. Finally, at pH 14, the NMR spectrum confirmed that substitution only occurred at the amine group with a DS of 0.75. At such a high pH, the amine group should act as a stronger nucleophile than the hydroxyl group [30], and a plausible mechanism for N-CM-chitosan formation is shown in Scheme 2.

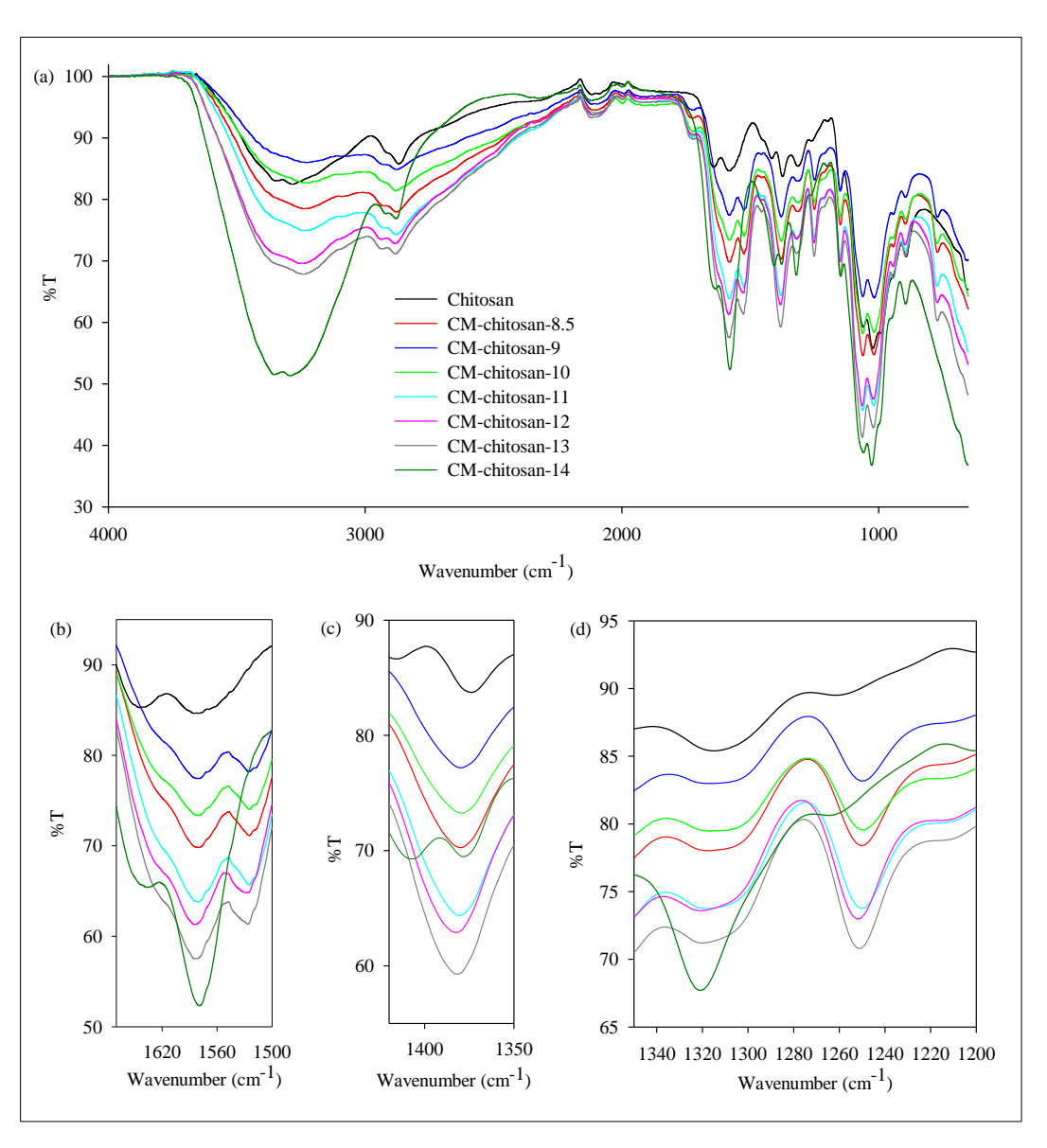


Figure 2. (a) Full FTIR-ATR spectra of chitosan and CM-chitosan derivatives. Enlarged spectra in the regions of (b) 1680–1500 cm<sup>-1</sup>, (c) 1420–1350 cm<sup>-1</sup>, and (d) 1360–1200 cm<sup>-1</sup>

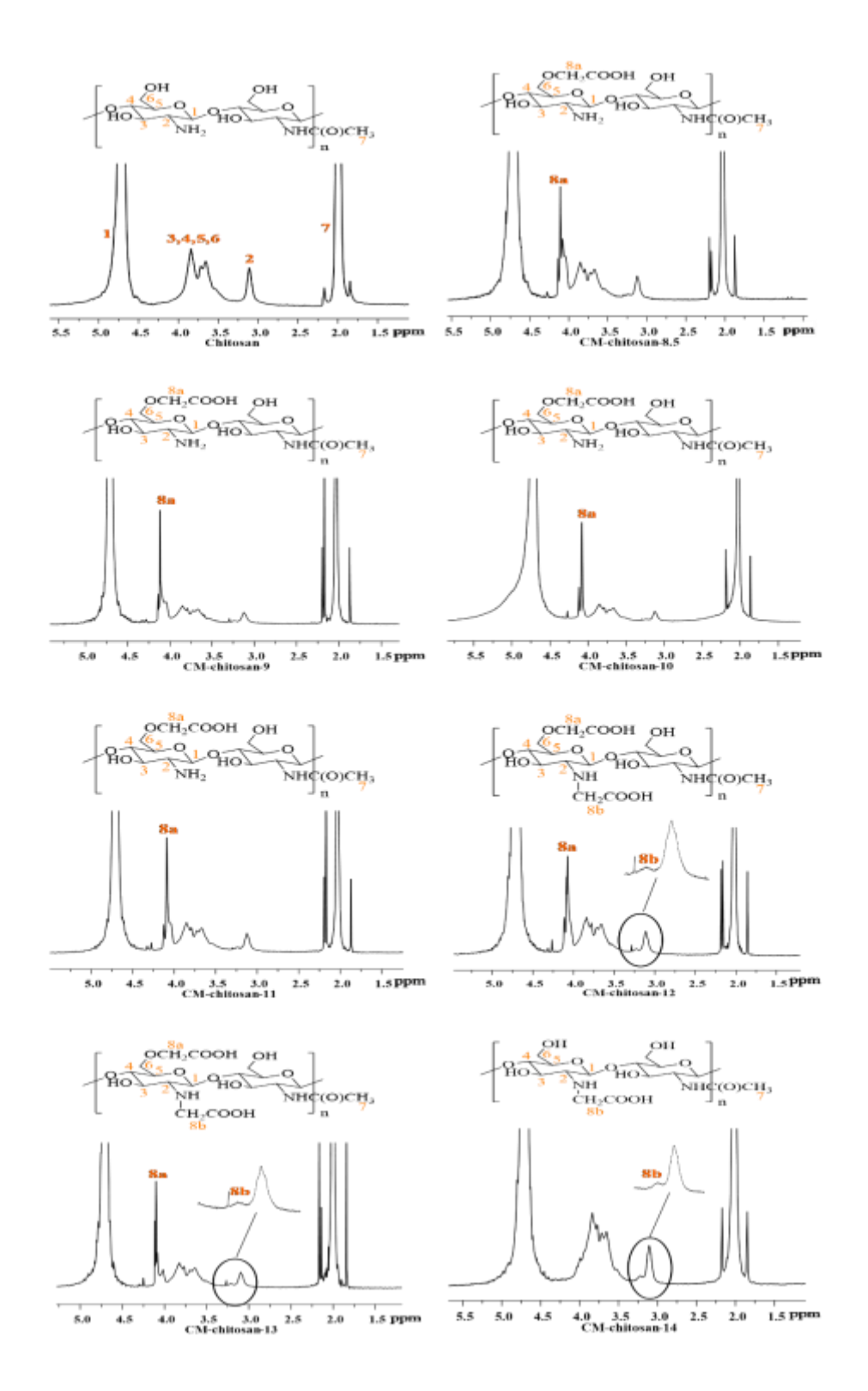


Figure 3. <sup>1</sup>H NMR spectra of chitosan and CM-chitosan derivatives

Table 1. DS values for CM-chitosan derivative synthesized at various pH values

Sample	DS
CM-chitosan-8.5	$0.80 \pm 0.10$
CM-chitosan-9	$0.81 \pm 0.12$
CM-chitosan-10	$0.78 \pm 0.12$
CM-chitosan-11	$0.70 \pm 0.10$
CM-chitosan-12	$0.80 \pm 0.10$
CM-chitosan-13	$0.66\pm1.10$
CM-chitosan-14	$0.75 \pm 0.26$

Scheme 1. Plausible mechanism for the synthesis of O-CM-chitosan from chitosan

Scheme 2. Plausible mechanism for the synthesis of N-CM-chitosan from chitosan

The student's t-test was used to observe the significance between pH selection and substitution site. pH values of 8.5-11 and pH 12-13 were selected as substitutions occurred at hydroxyl and amine groups, respectively. Based on the results, there were no significant differences in the DS values (p > 0.05), which showed that CM substitution can be carried out at the hydroxyl groups at pH 8.5-11 and the amine group at pH 12-13.

#### **Computational modeling studies**

The optimized structures of chitosan, O-CM-chitosan, N,O-CM-chitosan, and N-CM-chitosan are depicted in Figure 4. The structural optimization was performed at the B3LYP/6-31++G (d,p) level.

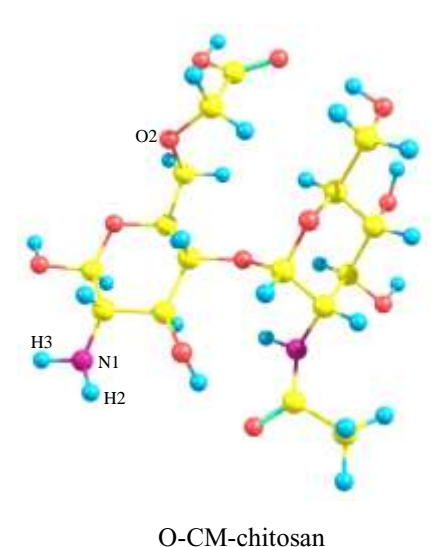
The Mulliken charges at O2, H1, N1, H2, and H3 of chitosan are shown in Table 2. The hydrogen atom at O2, which is H1, has a higher positive value than both the hydrogen atoms at N1, which are H2 and H3, because the oxygen atom is more electronegative than the nitrogen atom. As a result, the oxygen has a greater ability than the nitrogen atom to pull electrons from a hydrogen atom towards it.

Furthermore, the  $pK_a$  of oxygen is higher than that of nitrogen. The  $pK_a$  is a measure of how tightly a proton is held by an acid. Therefore, the electron density of the hydrogen bonded to oxygen decreased and the resulting increase in electropositivity made nucleophilic substitution of H1 easier than that of H2 or H3.

In addition, Mulliken charge values became more positive after CM group substitution. A similar outcome had been reported in a previous study. The study showed an increase of Mulliken charges for the structure with electron withdrawing substituents [31]. The Mulliken charge of O2 in O-CM-chitosan increased from -0.6334 to -0.2080, and a similar increase occurred for N1 in N-CM-chitosan (from -0.7153 to -0.2295). As shown in Table 2, the values for N,O-CM-chitosan were more positive, likely because the carboxylate groups, which are electron-withdrawing groups, were able to pull electrons from both the oxygen and nitrogen atoms [31]. However, the Mulliken charge not only affected the substituted atom, as the other atoms in the molecule also became more positive. Similar effects were observed for all the CM-chitosan derivatives. Previous study reported that this was due to the weakening of inter- and intramolecular hydrogen bonds after the introduction of CM groups [32].

The total energies of the chitosan and CM-chitosan derivative structures are illustrated in Figure 5. N,O-CM-chitosan has the lowest energy (-50796.31 eV) compared with chitosan, N-CM-chitosan, and O-CM-chitosan (-38378.67, -44595.38, and -44595.38 eV, respectively). Thus, among these structures, N,O-CM-chitosan is the most stable, likely because both the nucleophilic sites in N,O-CM-chitosan were substituted with a CM group, which made the structure less reactive and simultaneously increased the stability.





## Nur Ellina Annisa et al: SITE-SELECTIVE CARBOXYMETHYLATION OF CHITOSAN UNDER HETEROGENEOUS CONDITIONS

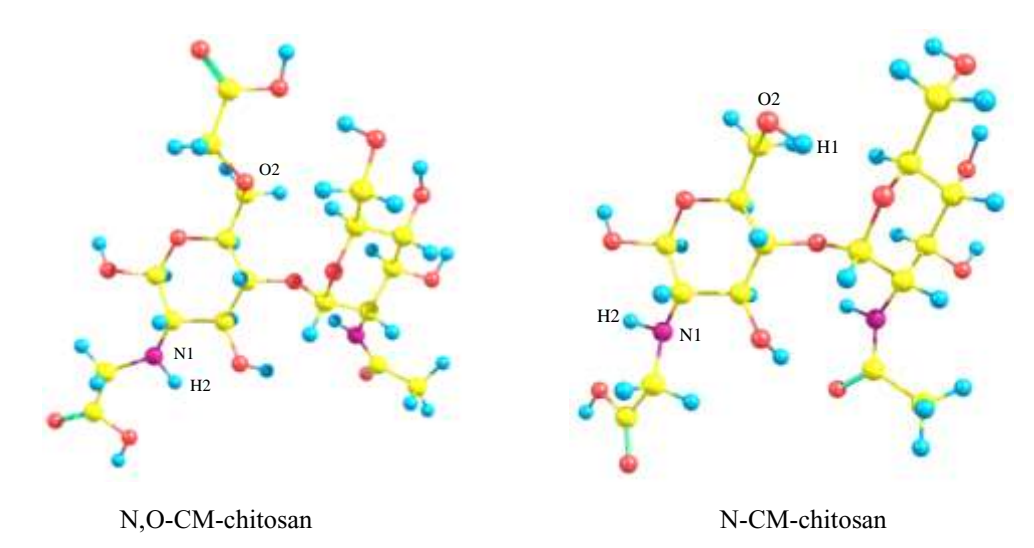


Figure 4. Optimized structures of chitosan and CM-chitosan derivatives (yellow: carbon; blue: hydrogen; red: oxygen; purple: nitrogen)

Table 2. Mulliken charges of atoms in chitosan and CM-chitosan derivative structures

Atom	Mulliken charges			
Atom	Chitosan	O-CM-chitosan	N,O-CM-chitosan	N-CM-chitosan
O2	-0.6334	-0.2080	-0.1871	-0.4152
H1	0.3977	-	-	0.4555
N1	-0.7153	-0.4480	-0.1356	-0.2295
H2	0.2918	0.3002	0.3880	0.3755
Н3	0.2984	0.3376	-	-

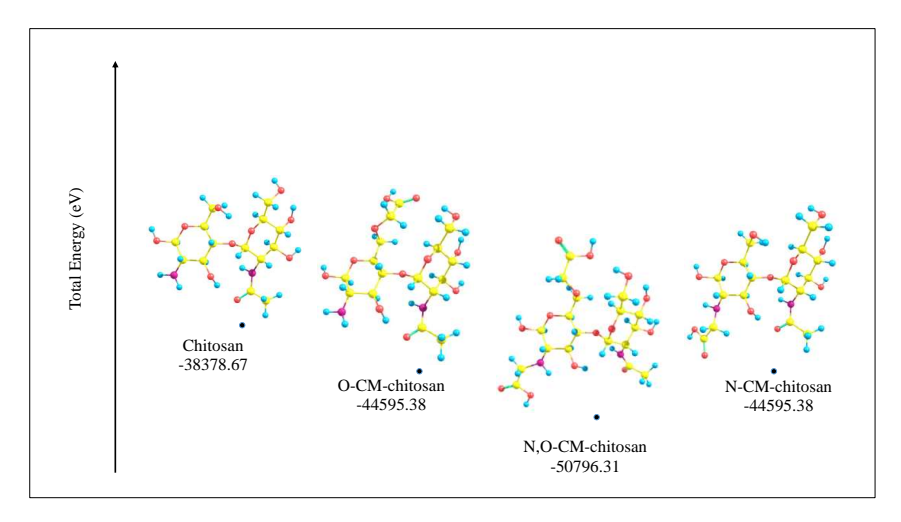


Figure 5. Total energies of chitosan and CM-chitosan derivative structures

#### Conclusion

In this study, CM-chitosan was successfully prepared under various pH conditions, as confirmed by FTIR-ATR spectroscopy, <sup>1</sup>H NMR spectroscopy, and DS calculations. Furthermore, computational modeling showed that the N,O-CM-chitosan structure was more stable than the O-CM-chitosan and N-CM-chitosan structures. The findings from this study make a noteworthy contribution to understanding the site-selectivity of chitosan substitution reactions under heterogeneous conditions. Under heterogeneous conditions, O-CM-chitosan was successfully obtained at pH 8.5–11, N,O-CM-chitosan at pH 12–13, and N-CM-chitosan at pH 14.

#### Acknowledgement

The authors would like to thank Universiti Kebangsaan Malaysia (UKM) for providing the facilities and research grant GGPM-2017-093.

#### References

- 1. Zhao, D., Yu, S., Sun, B., Gao, S., Guo, S. and Zhao, K. (2018). Biomedical applications of chitosan and its derivative nanoparticles. *Polymers*, 10(4): 462.
- 2. Wang, W., Meng, Q., Li, Q., Liu, J., Zhou, M., Jin, Z. and Zhao, K. (2020). Chitosan derivatives and their application in biomedicine. *International Journal of Molecular Sciences*, 21(2): 487.
- Kalliola, S., Repo, E., Srivastava, V., Zhao, F., Heiskanen, J. P., Sirviö, J. A., Liimatainen, H. and Sillanpää, M. (2018). Carboxymethyl chitosan and its hydrophobically modified derivative as pHswitchable emulsifiers. *Langmuir*, 34(8): 2800-2806.
- Rayung, M., Aung, M. M., Azhar, S. C., Abdullah, L. C., Su'ait, M. S., Ahmad, A., and Jamil, S. N. A. M. (2020). Bio-based polymer electrolytes for electrochemical devices: Insight into the ionic conductivity performance. *Materials*, 13(4): 838.
- Zhang, E., Xing, R., Liu, S., Li, K., Qin, Y., Yu, H., and Li, P. (2017). Comparison in docetaxel-loaded nanoparticles based on three different carboxymethyl chitosans. *International Journal of Biological Macromolecules*, 101: 1012–1018.
- 6. Aranaz, I., Acosta, N., Civera, C., Elorza, B.,

- Mingo, J., Castro, C., Gandía, M. D. L. L. and Caballero, A. H. (2018). Cosmetics and cosmeceutical applications of chitin, chitosan and their derivatives. *Polymers*, 10(2): 213.
- 7. Jimtaisong, A. and Saewan, N. (2014). Utilization of carboxymethyl chitosan in cosmetics. *International Journal of Cosmetic Science*, 36(1): 12–21.
- Zhong, H., He, A., Lu, J., Sun, M., He, J. and Zhang, L. (2016). Carboxymethyl chitosan/conducting polymer as water-soluble composite binder for LiFePO<sub>4</sub> cathode in lithium ion batteries. *Journal of Power Sources*, 336: 107-114.
- Sun, S. and Wang, A. (2006). Adsorption kinetics of Cu(II) ions using N,O-carboxymethyl-chitosan. *Journal of Hazardous Materials*, 131(1–3): 103-111.
- Mi, Y., Su, R., Fan, D., Zhu, X. and Zhang, W. (2013). Preparation of N,O-carboxymethyl chitosan coated alginate microcapsules and their application to *Bifidobacterium Longum* BIOMA 5920. *Materials Science and Engineering: C*, 33(5): 3047-3053.
- 11. Muzzarelli, R. A. A., Tanfani, F., Emanuelli, M. and Mariotti, S. (1982). N-(carboxymethylidene)chitosans and N-(carboxymethyl)chitosans: Novel chelating polyampholytes obtained from chitosan glyoxylate. *Carbohydrate Research*, 107(2): 199-214.
- Nudga, L. A., Plisko, E. A. and Danilov, S. N. (1973). N-alkylation of chitosan. *Zhurnal Obshchei Khimii*, 43(12): 2756-2760.
- An, N. T., Dung, P. L., Thien, D. T., Dong, N. T. and Nhi, T. T. Y. (2008). An improved method for synthesizing N,N'-dicarboxymethylchitosan. *Carbohydrate Polymers*, 73(2): 261-264.
- An, N. T., Dung, P. L., Thien, D. T., Dong, N. T. and Nhi, T. T. Y. (2009). Water-soluble N-carboxymethylchitosan derivatives: preparation, characteristics and its application. *Carbohydrate Polymers*, 75(3): 489-497.

### Nur Ellina Annisa et al: SITE-SELECTIVE CARBOXYMETHYLATION OF CHITOSAN UNDER HETEROGENEOUS CONDITIONS

- 15. Nikmawahda, H. T., Sugita, P., and Arifin, B. (2015). Synthesis and characterization of nalkylchitosan as well as its potency as a paper coating material. *Advances in Applied Science Research*, 6(2): 141-149.
- Sashiwa, H., Shigemasa, Y., and René, R. (2000).
   Novel N-alkylation of chitosan via michael type reaction. *Chemistry Letters*, 29(8): 862-863.
- 17. Sun, G., Chen, X., Li, Y., Zheng, B., Gong, Z., Sun, J., Chen, H., Li, J. and Lin, W. (2008). Preparation of H-oleoyl-carboxymethyl-chitosan and the function as a coagulation agent for residual oil in aqueous system. *Frontiers of Materials Science in China*, 2(1): 105-112.
- Leong, K. H., Chung, L. Y., Noordin, M. I., Mohamad, K., Nishikawa, M., Onuki, Y., Morishita, M., and Takayama, K. (2011). Carboxymethylation of kappa-carrageenan for intestinal-targeted delivery of bioactive macromolecules. *Carbohydrate Polymers*, 83(4): 1507-1515.
- 19. Singh, R. K. and Khatri, O. P. (2012). A scanning electron microscope based new method for determining degree of substitution of sodium carboxymethyl cellulose. *Journal of Microscopy*, 246(1): 43-52.
- 20. Elomaa, M., Asplund, T., Soininen, P., Laatikainen, R., Peltonen, S., Hyvärinen, S. and Urtti, A. (2004). Determination of the degree of substitution of acetylated starch by hydrolysis, <sup>1</sup>H NMR and TGA/IR. *Carbohydrate Polymers*, 57(3): 261-267.
- 21. Aggeryd, I., and Olin, Å. (1985). Determination of the degree of substitution of sodium carboxymethylcellulose by potentiometric titration and use of the extended henderson-hasselbalch equation and the simplex method for the evaluation. *Talanta*, 32(8A): 645-649.
- Liu, J., Zhang, X., Kennedy, J. F., Jiang, M., Cai, Q. and Wu, X. (2019). Chitosan induces resistance to tuber rot in stored potato caused by *Alternaria* tenuissima. International Journal of Biological Macromolecules, 140: 851-857.
- Mobarak, N. N., Ahmad, A., Abdullah, M. P., Ramli, N. and Rahman, M. Y. A. (2013). Conductivity enhancement via chemical modification of chitosan based green polymer

- electrolyte. Electrochimica Acta, 92: 161-167.
- 24. Lusiana, R. A., Siswanta, D. and Mudasir, M. (2014). Modifying surface charge of chitosan membrane by N,O-carboxymethyl chitosan blended with poly(vinyl alcohol). *International Journal of Advances in Chemical Engineering and Biological Sciences*, 1(1): 16-20.
- 25. Hirai, A., Odani, H. and Nakajima, A. (1991). Determination of degree of deacetylation of chitosan by <sup>1</sup>H NMR spectroscopy. *Polymer Bulletin*, 26(1): 87-94.
- Muzzarelli, R. A. A., Ilari, P., and Petrarulo, M. (1994). Solubility and structure of N-carboxymethylchitosan. *International Journal of Biological Macromolecules*, 16(4): 177-180.
- 27. Prabaharan, M. and Gong, S. (2008). Novel thiolated carboxymethyl chitosan-g-β-cyclodextrin as mucoadhesive hydrophobic drug delivery carriers. *Carbohydrate Polymers*, 73 (1): 117-125.
- 28. Chen, X. G. and Park, H. J. (2003). Chemical characteristics of o-carboxymethyl chitosans related to the preparation conditions. *Carbohydrate Polymers*, 53(4): 355-359.
- Bukzem, A. L., Signini, R., Dos Santos, D. M., Lião, L. M. and Ascheri, D. P. R. (2016). Optimization of carboxymethyl chitosan synthesis using response surface methodology and desirability function. *International Journal of Biological Macromolecules*, 85: 615-624.
- 30. Mourya, V.., Inamdar, N. N. and Tiwari, A. (2010). Carboxymethyl chitosan and its applications. *Advanced Materials Letters*, 1(1): 11-33.
- 31. Pranowo, H. D., Mulya, F., Aziz, H. A, and Santoso, G. A. (2018). Study of substituent effect on properties of platinum(II) porphyrin semiconductor using density functional theory. *Indonesian Journal of Chemistry*, 18(4): 742-748.
- 32. Lu, X., Xue, J. Q., Wang, Y. J., Mao, W. B., Wu, M. and Li, J. X. (2010). Theoretical studies on the chemical structure of carboxymethyl chitosan. *Advanced Materials Research*, 160-162: 1822-1827.

# Malaysian Journal of Analytical Sciences (MJAS) Published by Malaysian Analytical Sciences Society

# CLASSIFICATION MODEL FOR DETECTION AND DISCRIMINATION OF INEDIBLE PLASTIC ADULTERATED PALM COOKING OIL USING ATR-FTIR SPECTROSCOPY COMBINED WITH PRINCIPAL COMPONENT ANALYSIS

(Model Pengkelasan bagi Pengesanan dan Pengasingan Produk Cemaraduk Plastik dalam Minyak Masak Sawit Menggunakan Spektroskopi ATR-FTIR dengan Gabungan Analisis Komponen Prinsipal)

Dzulkiflee Ismail<sup>1</sup>, Aliyalina Rahimi<sup>1</sup>, Wan Rosli Wan Ishak<sup>2</sup>, Naji Arafat Mahat<sup>3</sup>, Wan Nur Syuhaila Mat Desa<sup>1\*</sup>

<sup>1</sup> Forensic Science Programme, School of Health Sciences
<sup>2</sup> Nutrition Programme, School of Health Sciences
Universiti Sains Malaysia, Health Campus, 16150 Kubang Kerian, Kelantan, Malaysia
<sup>3</sup>Department of Chemistry, Faculty of Science,
Universiti Teknologi Malaysia, 81310 Skudai, Johor, Malaysia

\*Corresponding author: wannurs@usm.my

Received: 17 March 2021; Accepted: 28 May 2021; Published: 27 June 2021

#### Abstract

Adulteration of edible oil by replacing or admixing cheaper or waste oil is an irresponsible act motivated by profiteering. A more sinister act of dissolving inedible plastic materials in hot oil during frying to enhance the crispiness and prolong the shelf life of deep-fried snacks has been alleged. In this study, a protocol using ATR-FTIR spectroscopy combined with principal component analysis (PCA) for detection of inedible plastic materials in palm cooking oil is presented. To achieve this, palm cooking oil samples purchased from convenience stores were heated and adulterated either with low-density polyethylene (LDPE), high-density polyethylene (HDPE) or polypropylene (PP). The resultant spectra from 4000-600 cm<sup>-1</sup> were subjected to direct visual examinations prior to PCA. Detection of plastic materials in the samples from direct visual examinations of the resultant spectra was difficult as all samples revealed similar spectra dominated by major absorption bands at 2922 cm<sup>-1</sup>, 2853 cm<sup>-1</sup>, 1740 cm<sup>-1</sup>, 1465 cm<sup>-1</sup>, 1377 cm<sup>-1</sup> and 721 cm<sup>-1</sup>, which were typical of triacylglycerols. Despite the similarities, the detection was possible when the resultant spectra were subjected to PCA. The results demonstrated the potential of ATR-FTIR spectroscopy combined with PCA for the detection of inedible plastic adulterated palm cooking oil.

**Keywords:** ATR-FTIR spectroscopy, cooking oil, adulteration, polyethylene, polypropylene

#### Abstrak

Cemaraduk minyak makan dengan menggantikan atau mencampurkan bersama minyak murah atau minyak sisa adalah tindakan tidak bertanggungjawab didorong oleh sikap meraih keuntungan. Tindakan yang lebih tidak bertanggungjawab adalah melarutkan plastik tidak boleh dimakan ke dalam minyak panas semasa menggoreng bertujuan untuk meningkatkan kerangupan dan

# Dzulkiflee et al: CLASSIFICATION MODEL FOR DETECTION AND DISCRIMINATION OF INEDIBLE PLASTIC ADULTERATED PALM COOKING OIL USING ATR-FTIR SPECTROSCOPY COMBINED WITH PRINCIPAL COMPONENT ANALYSIS

memanjangkan jangka hayat makanan gorengan telah diperkatakan. Kajian ini membentangkan protokol menggunakan kaedah spektroskopi ATR-FTIR yang digabungkan bersama analisis komponen prinsipal (PCA) untuk mengesan bahan plastik tidak boleh dimakan dalam minyak sawit goreng. Untuk mencapai matlamat ini, sampel minyak masak sawit dibeli dari kedai serbaneka telah dipanaskan dan diadukkan bersama polietilena ketumpatan rendah (LDPE), polietilena ketumpatan tinggi (HDPE) atau polipropilena (PP). Spektra inframerah yang diperoleh dari 4000-600 cm<sup>-1</sup> telah diperiksa terlebih dahulu melalui kaedah pemeriksaan visual langsung sebelum PCA. Pengesanan bahan plastik tidak boleh dimakan dalam semua sampel melalui kaedah pemeriksaan visual dari spektra inframerah yang dihasilkan adalah sukar berikutan kesemua sampel menghasilkan spektra serupa dengan jalur penyerapan utama tipikal triasilgliserol pada 2922 cm<sup>-1</sup>, 2853 cm<sup>-1</sup>, 1740 cm<sup>-1</sup>, 1465 cm<sup>-1</sup>, 1377 cm<sup>-1</sup> dan 721 cm<sup>-1</sup>. Walaupun terdapat persamaan, pengesanan dilakukan dengan jayanya menggunakan PCA. Hasil kajian menunjukkan potensi penggabungan spektroskopi ATR-FTIR bersama PCA untuk pengesanan plastik tidak boleh dimakan teraduk dalam minyak masak sawit.

Kata kunci: spektroskopi ATR-FTIR, minyak masak, pengadukan, polietilena, polipropilena

#### Introduction

Palm cooking oil is a popular choice for deep frying due to its excellent and versatile techno-economic advantages for almost all frying activities [1]. In certain South East Asia countries, deep-fried snacks such as deep-fried banana, deep-fried fish fritter and fried chicken are commonly found in street stalls sold by hawkers. Recently, the practise of adding and dissolving inedible plastic materials such as used plastic carrier bags, used plastic packaging and used straws into hot oil by irresponsible street hawkers prior to frying is rumoured. Purportedly, this practise helps to enhance the crispiness, as well as prolong the freshness and the shelf-life of deep-fried snacks [2]. If this allegation is true, such malpractice is undoubtedly alarming as it poses serious health implications to the consumers since a wide range of chemicals used in the manufacture of plastics such as bisphenol-A (BPA), melamine, thalates, antiminitroxide, brominated flame retardants and polyfluorinated chemicals are known to be toxic [3,4]. Among health problems associated with toxins found in plastics are liver dysfunction, cancers, skin diseases, neuro-toxicity, lung problems and gastrointestinal issues [3, 4]. This malicious practice which is undoubtedly a serious food safety issue warrants the development of a sensitive detection technique, capable of detecting dissolved inedible plastic materials.

Infrared (IR) spectroscopy has emerged as one of the useful analytical tools for monitoring food safety issues. In order to further enhance its detection ability, it is often combined with chemometrics techniques [5, 6]. This

hybrid approach has been used, among others to detect the adulteration of extra virgin olive oil with sunflower, peanut, canola, corn, sunflower and soybean oil [7], the adulteration of high-priced walnut oil with low-priced sunflower and soybean oil [8], the presence of chicken fat in butters [9], the adulteration of rapeseed oil with waste cooking oil [10], the presence of lard in French fries pre-fried in palm oil adulterated with lard [11] and the adulteration of *pekmez*, a Turkish sweet with glucose syrup, high fructose corn syrup and other sugars [5].

IR spectroscopy is a spectroscopy technique that uses the electromagnetic radiation within the IR region. When transmitted through a sample, electromagnetic radiation stimulates vibrational motions of the molecules within the sample [6, 12]. When the vibration of a molecule matches with the frequency of the transmitted IR radiation, a spectral band or peak is produced. Different molecules absorb IR radiation at different frequencies, hence producing different spectral bands characteristic which are useful for identification. Early IR spectrophotometers require tedious sample preparation. With the advancement of technology, attenuated total reflectance (ATR) attachment is introduced. This attachment has revolutionized FTIR spectroscopy which allows for direct in-situ, straightforward sample analysis with minimal to no sample pre-treatment requirement.

Principal Component Analysis (PCA) is one of the chemometrics techniques that has been used to monitor and detect adulterants in food. This particular

chemometrics technique allows large sample of data sets to be described using a much smaller number of principal components or PCs. The first PC, known as PC1 describes the gross average features of the data sets while the second PC, or PC2, and the subsequent PCs introduce further specific features of decreasing significance [13, 14]. PCA is a suitable tool for simplification, data reduction, outlier detection and pattern recognition highlighting the variance or differences within a dataset. In the case of PCA performed on a FTIR spectra, it allows the investigation of trends in the studied samples and relationships or differences between samples.

As far as this study is concerned, no work has been done focussing on the detection of plastic adulterated cooking oil using ATR-FTIR spectroscopy combined with PCA. Therefore, in this study, the authors intend to demonstrate the use of this hybrid approach for the detection and discrimination of inedible plastic in palm cooking oil.

#### **Materials and Methods**

#### Sample collection

New and unused 1 kg refined palm cooking oils (RCO) (n = 6) of similar brand were purchased from a local convenience store over a period of 6 months while low-density polyethylene (PE1), high-density polyethylene (PE2) and polypropylene (PP) plastic bags were purchased directly from a plastic bag retail store to reflect the alleged field practice. Fresh bananas purchased from the local market were selected as the item to fry because it was an easy local snack to prepare compared to other processed foods such as chicken meats. The heating and cooking procedures were conducted using a stainless-steel frying pan (Zebra Inc., Thailand) and a portable cooking stove (Power Plus, China) equipped with a portable butane gas canister (Chelstar, Korea).

#### Sample preparation

Each packet of 1 kg (equivalent to approximately 1200 mL) (n=6) RCO was divided to five equal portions to prepare for control unadulterated (URCO), heated refined oil (HRCO), heated with food (HRCOB), adulterated without food (ARCO, referred as RCO-PE1,

RCO-PE2 and RCO-PP according to the plastic materials used to adulterate them) and adulterated with food (ARCOB, referred as ARCO-B-PE1, ARCO-B-PE2 and ARCO-B-PP according to the plastic materials used to adulterate them) oil sets.

HRCO (n=5) was prepared by heating approximately 400 mL of control cooking oil to approximately 200 °C (K-type digital thermocouple, MYPIN, China) until small bubbles and thin white smoke were released. The heating time to achieve the condition was about 2 minutes. Once heating was completed, sample was allowed to stand to cool off at room temperature at approximately 25 °C.

Adulterated oil samples without food (ARCO) (n=5) were prepared by gradually dissolving approximately four grams of PE1 strips into hot RCO as previously described. The amount of plastic incorporated reflects the average weight of one plastic bag. Similar procedures were repeated for PE2 and PP plastic materials.

For HRCOB (n=5) and ARCOB (n=5) samples, slices of banana were fried for 2 minutes each under a similar setup. Upon cooling, the oil samples from each set were filtered using a filter paper (Whatman, Merck, Germany). Approximately 2 mL of the filtered oil was then transferred into a separate half dram glass vial (Bischem, Malaysia) and kept at 4°C in refrigerator prior to subsequent ATR-FTIR analysis.

#### **ATR-FTIR** analysis

The IR spectra were obtained using a Bruker Tensor 27 FTIR spectrometer (Bruker Technologies, USA) equipped with a zinc selenide (ZnSe) ATR sampling interface. The instrument control and data acquisition were operated by OPUS Ver. 7.0.122 software (Bruker, Germany). To check for detection accuracy, the FTIR spectrometer was calibrated against a standard polystyrene film (Bruker Optics, Germany). All IR spectra were obtained in the frequency region of 4000-600 cm<sup>-1</sup> where 16 scans were collected at a resolution of 4 cm<sup>-1</sup>.

# Dzulkiflee et al: CLASSIFICATION MODEL FOR DETECTION AND DISCRIMINATION OF INEDIBLE PLASTIC ADULTERATED PALM COOKING OIL USING ATR-FTIR SPECTROSCOPY COMBINED WITH PRINCIPAL COMPONENT ANALYSIS

Sample IR spectra acquisition was performed by placing a drop of oil sample on the surface of the ZnSe sampling interface. Once measurement had been completed, the oil sample was removed from the interface using dry tissues (Kimberly Clark, UK) and subsequently was wiped again using a clean tissue soaked with methanol before and after each analysis. The plastic materials were also measured in ATR mode. Confirmation of the IR profiles of the plastic materials used as the adulterants were accomplished by comparison with literature references [15]. Spectrum acquisition for each sample was performed in six replicates at room temperature (25 °C).

#### Sample variations

In this study, variations within and between samples were assessed through repeatability and reproducibility measurements respectively using the URCO as the samples. The former was measured by conducting six consecutive measurements or spectra acquisitions on one of the URCO samples while the latter was measured by conducting one measurement to each of the six batches of the URCO samples. Both repeatability and reproducibility were expressed using relative standard deviation (%RSD) which is defined as the percentage ratio of standard deviation over mean or average of below than 5% as stated by international analytical guidelines [15].

### Data pre-processing and principal component analysis

The resultant IR spectra were converted to commaseparated values (.CSV) format prior to importing to the Excel spreadsheet (Microsoft, USA) for further data preparation and pre-processing. A series of data pre-processing strategies which were auto-scaling, column centring and square root transformation were applied to the IR data matrices. Once the series of data pre-processing were completed, the pre-processed IR data matrices were imported to Minitab Version 16.2.3 statistical software (Minitab Inc., USA) environment for principal component analysis (PCA). Assessment of the ability of PCA to detect and discriminate the non-plastic adulterated oil from its non-adulterated counterparts was made based on score plots observations in which the

principal component (PC) score plots were constructed using the first two resultant principal components.

#### **Results and Discussion**

In this study, the %RSD for both repeatability and reproducibility were computed using the absorbances recorded by six prominent peaks manually selected from the IR spectra of the URCO oil samples. The %RSD for repeatability recorded for the six prominent peaks at 2922.01 cm<sup>-1</sup>, 2852.27 cm<sup>-1</sup>, 1743.56 cm<sup>-1</sup>, 1463.89 cm<sup>-1</sup>, 1159.16 cm<sup>-1</sup> and 721.34 cm<sup>-1</sup> were 0.45%, 0.44%, 0.28%, 0.27%, 1.77% and 0.24% respectively while their %RSD for reproducibility were 0.57%, 0.63%, 0.44%, 0.57%, 0.66% and 0.88%, respectively. Following the analytical guideline mentioned earlier, the low percentage of these %RSD values indicated good repeatability and reproducibility of the analyses.

#### ATR-FTIR spectral analysis of the plastic materials

The IR spectra of PE1, PE2 and PP used as the adulterants are shown in Figure 1 to Figure 3 respectively. Close manual visual examinations of PE1 and PE2 IR spectra in Figure 1 and Figure 2 revealed similar absorption peaks occurring at ~2910 cm<sup>-1</sup> which corresponds to C-CH<sub>3</sub> and ~2843 cm<sup>-1</sup> corresponding to CH<sub>2</sub>. Methylene deformations i.e. CH<sub>2</sub> vibrations were observed at ~1460 cm<sup>-1</sup> and ~720 cm<sup>-1</sup> due to their bending vibrations [16]. The difference in the degree of branching within PE1 and PE2 structures could possibly accounts for different proportions of peak intensity. The spectrum of PP shown in Figure 3 revealed characteristic absorption bands in the functional group with a more complicated absorption band in the fingerprint regions in comparison to PE due to different monomer build-up of propene (C<sub>3</sub>H<sub>6</sub>) in PP plastic such as the addition of a methyl side group. Characteristic split peaks at ~2954 cm<sup>-1</sup> and ~2914 cm<sup>-1</sup> correspond to methyl groups while ~2866-2835 cm<sup>-1</sup> designates the CH groups within the sample. The complicated PP fingerprint region with weak absorption band within ~1160 cm<sup>-1</sup> and ~790 cm<sup>-1</sup> regions showed vibration characteristic of polypropylene. Table 1 to Table 3 detail out the absorption peaks and the corresponding functional groups recorded for PE1, PE2 and PP respectively. These absorption peaks are in conformance

to those described by Asensio et al. [14] and Moinuddin [17].

### ATR-FTIR spectral analysis of the cooking oil samples

Triacylglycerols (TAGs) are the major organic compounds of oils and fats of plant origin including palm oil, therefore they dominate the spectra as seen in Figure 4. The IR spectra of the samples including those adulterated with the plastic materials show that there were several absorption bands in the functional group regions compared to the absorption bands in the fingerprint region. Strong absorption bands were observed in the region of 3000-2800 cm<sup>-1</sup> caused by C-H stretching vibrations. Bands at 3009 cm<sup>-1</sup> correspond to the stretching vibration of C=H. The stretching vibration of methylene (-CH<sub>2</sub>-) and methyl (-CH<sub>3</sub>) functional groups can be seen at 2922 cm<sup>-1</sup> and 2853 cm<sup>-</sup> <sup>1</sup>, respectively. Methylene and methyl groups were also observed at 1465 cm<sup>-1</sup> and 1377 cm<sup>-1</sup> due to their bending vibrations [16] The sharp peak around 1740 cm<sup>-</sup> <sup>1</sup> was due to C=O double bond stretching vibration. Deformation and bending of C-H and stretching vibration of C-O result in peaks at 1500-650 cm<sup>-1</sup> region [17-19]. The functional groups associated with the absorption peaks identified from the spectra of the cooking oil samples are summarised in Table 4.

In general, the oil spectra in Figure 4 did not show any major differences between them. Further examination on the fingerprint regions (between 1500-600 cm<sup>-1</sup>) also revealed a similar spectral pattern with a very minimal shift of absorption band positions and intensity across the samples despite the inclusion of plastic adulterants and further subdued under different conditions. These samples may have undergone a different degree of chemical reactions after adulteration. Furthermore, during cooking, hydrolysis, oxidation, polymerisation and isomerisation reactions are inevitable thus may have resulted in the multitude of assorted by-products [14, 17]. Hence, it is postulated that those chemical reactions may bring evident changes to the spectra especially between the unadulterated cooking oils (URCO and HRCO) and the plastic adulterated cooking oils (ARCO-PE1, ARCO-PE2 and ARCO-PP), however this is not the case. Perhaps the changes due to those reactions are significantly small which explain the subtle differences between the spectra which have hampered the differentiation of the samples by direct visual examination and recognition. Furthermore, since the manual visual examination is subjective, it is therefore practical to incorporate statistical methods which can aid in explaining the differences between the cooking oil samples or in other words, capture the differences between the samples.

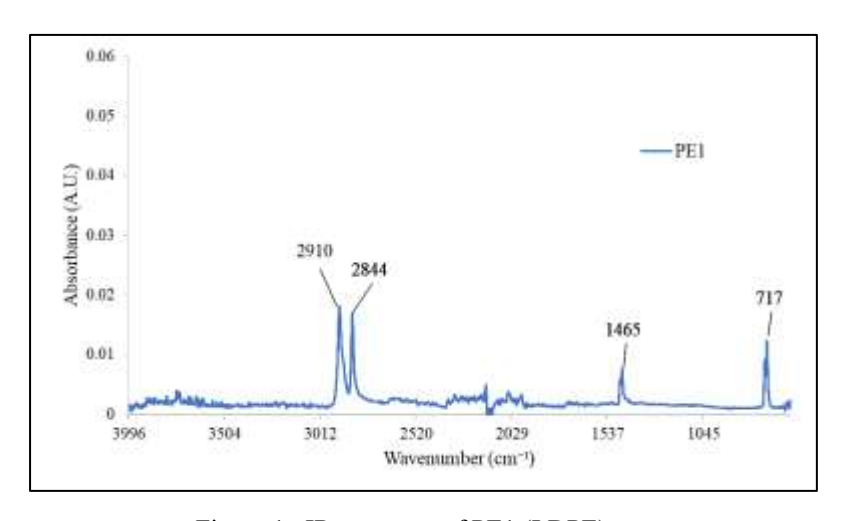


Figure 1. IR spectrum of PE1 (LDPE)

# Dzulkiflee et al: CLASSIFICATION MODEL FOR DETECTION AND DISCRIMINATION OF INEDIBLE PLASTIC ADULTERATED PALM COOKING OIL USING ATR-FTIR SPECTROSCOPY COMBINED WITH PRINCIPAL COMPONENT ANALYSIS

Table 1. The functional groups associated with absorption peaks identified in PE1

Absorption Peak (cm <sup>-1</sup> )	Functional Group
2910	C-CH <sub>3</sub>
2844	$CH_2$
1465	CH <sub>3</sub>
717	-CH=CH-(cis)

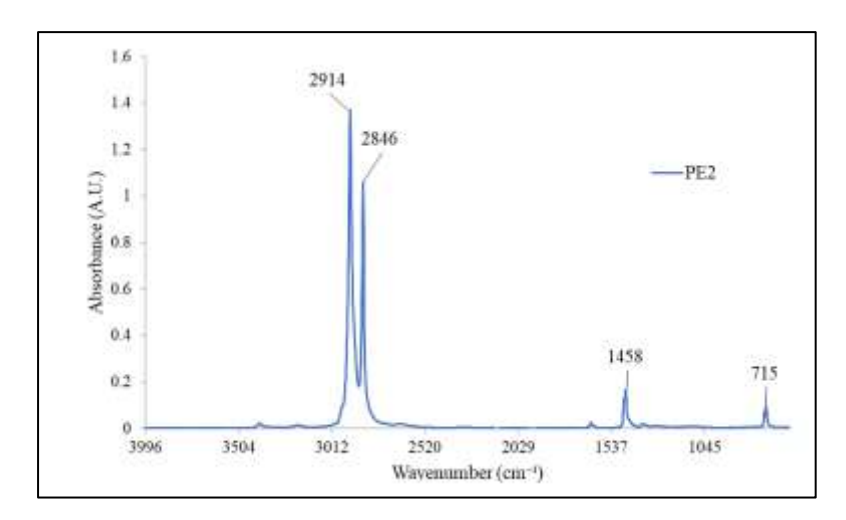


Figure 2. IR spectrum of PE2 (HDPE)

Table 2. The functional groups associated with absorption peaks identified in PE2

Absorption Peak (cm <sup>-1</sup> )	Functional Group
2914	C-CH <sub>3</sub>
2846	$CH_2$
1458	CH <sub>3</sub>
715	-CH=CH-(cis)

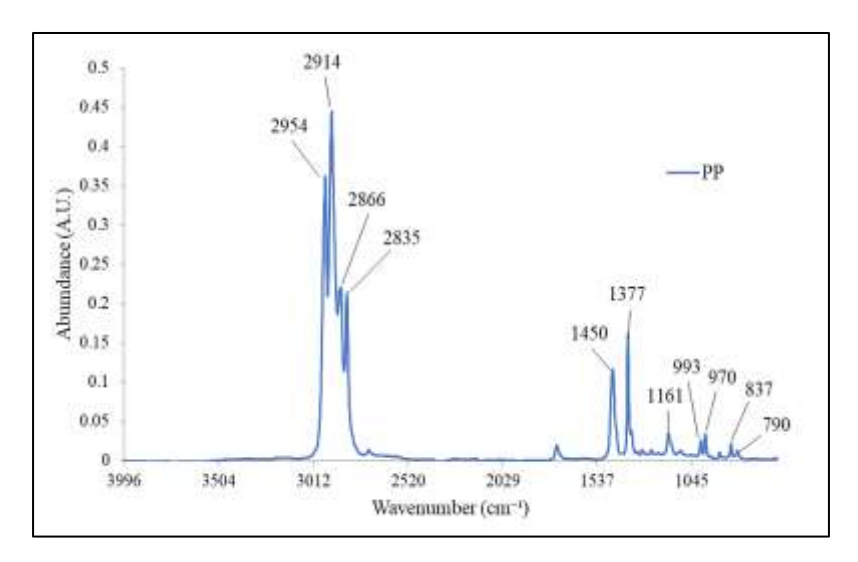


Figure 3. IR Spectrum of PP

Table 3. The functional groups associated with absorption peaks identified in PP

Absorption Peak (cm <sup>-1</sup> )	Functional Group
2954	C-CH <sub>3</sub>
2914	C-CH <sub>3</sub>
2866	$CH_2$
2835	$CH_2$
1450	CH <sub>3</sub>
1377	CH <sub>3</sub>
1161	Acetates
993	-CH=CH <sub>2</sub>
970	-CH=CH- (trans)
837	C=CH <sub>2</sub>
790	-CH=CH-(cis)

## Data pre-processing and principal component analysis

Prior to applying PCA, the IR spectra of the oil samples were pre-processed using a series of pre-processing techniques previously mentioned in the pre-processing section, aiming to minimise data variation due to run-to-run variation and to overcome the dominating effect of strong peak absorbance over weaker absorbance intensity. The entire IR spectrum region from 4000-600 cm<sup>-1</sup> with 3401 variables would be the best option for

performing PCA, however due to its extremely large number of variables, it limits the software's ability to execute the principal component analysis. Since the frequency region from 4000 cm<sup>-1</sup>-1501 cm<sup>-1</sup> did not carry much information as evident in Figure 4, and to overcome the limitation associated with the software, it was decided to focus only on the characteristic fingerprint region (from 1500-600 cm<sup>-1</sup>). This approach was sensible as unlike the frequency region, the fingerprint region carries more useful information as

# Dzulkiflee et al: CLASSIFICATION MODEL FOR DETECTION AND DISCRIMINATION OF INEDIBLE PLASTIC ADULTERATED PALM COOKING OIL USING ATR-FTIR SPECTROSCOPY COMBINED WITH PRINCIPAL COMPONENT ANALYSIS

evident in Figure 4 which corroborates with prior information [13,14]. Additionally, it has a much lower number of variables (901 variables), which has proven to be beneficial in reducing the computational burden of the software. Subsequently, pre-processing and PCA were performed on the fingerprint regions.

A large number of PCA score plots had been generated in this study from the pairwise combinations of specific fingerprint region with different pre-processing strategies. However, for simplicity of discussion, only PCA score plot that has generated the easiest interpretable outcome i.e. score plot of square root transformed is reported here. Figure 5 shows the PCA score plot of the square root transformed dataset plotted using the first two principal components, namely PC1 and PC2. The former PC explains 67.2% of the variation or variability in the dataset while the second PC explains 14.8% of the variation in the dataset. The combination of these two PCs hence explains 81.8% (PC1 = 67.2% + PC2 = 14.6% = 81.8%) of the variation in the dataset which means that the PCA has adequately captured relevant information within the dataset.

Close examinations of the PCA score plot reveal nine neat clusters or groupings (designated as cluster A, B, C, D, E, F, G, H and I) associated with each of the nine cooking oil samples in this study which can be divided into two hyperplanes. Cooking oil samples without plastic materials are clustered into three separate clusters, identified as cluster A (U-RCO), B (H-RCO) and C (H-RCO-B) at the lower region of the score plot. The cooking oil samples which contained or were adulterated with plastic materials only are also clustered into three clusters as shown by cluster D (RCO-PE1), E (RCO-PE2) and F (RCO-PP) at the upper region of the score plot spanning from left to the upper centre of the plot. It is particularly interesting to note that cooking oil samples containing plastic materials which were used to fry the bananas are also clustered into three separate clusters as cluster G (ARCO-B-PE1), H (ARCO-B-PE2) and I (ARCO-B-PP) at a position away from the rest of the cooking oil samples. This rather interesting finding indicates the capability of this hybrid approach for monitoring cooking oil adulterated with plastic materials which are not intended for human consumption.

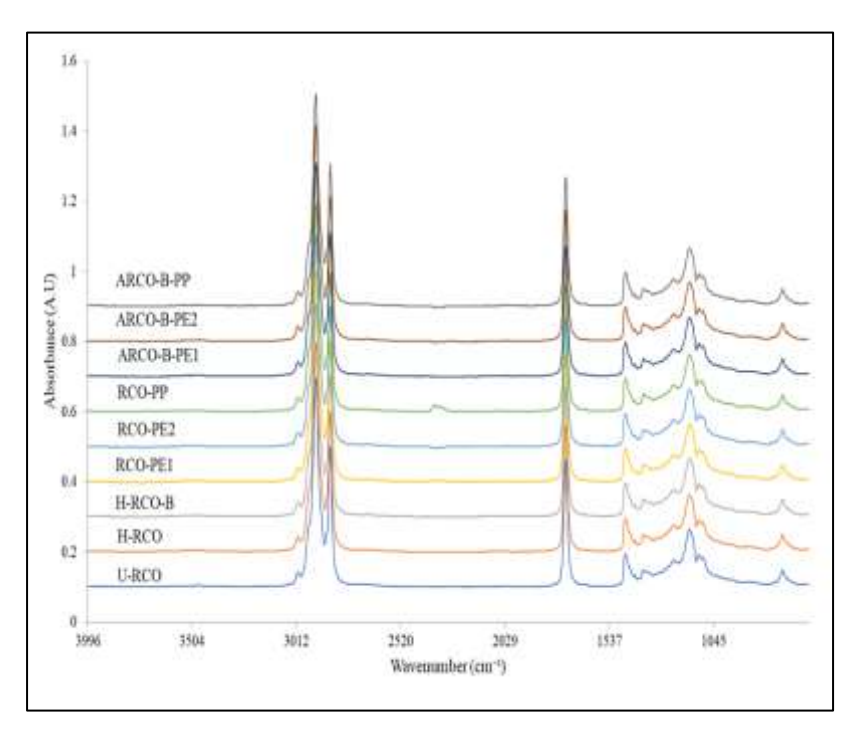


Figure 4. FTIR spectra of the cooking oil samples.

Table 4. The major peaks found in the spectra of the cooking oil samples and their corresponding functional groups [17]

Wavenumber (cm <sup>-1</sup> )	Peak Assignment	
3009	C-H stretching vibration of the cis-double bond (=CH)	
2960	Symmetric and asymmetric stretching vibration shoulder of the aliphatic CH <sub>3</sub> group	
2852, 2920	Symmetric and asymmetric stretching vibration of the aliphatic CH2 group	
1743	Ester carbonyl functional group of the triglycerides	
1465	Bending vibrations of the CH <sub>2</sub> and CH <sub>3</sub> aliphatic groups	
1377	Bending vibrations of CH <sub>2</sub> groups	
1098, 1117, 1160, 1236	Stretching vibration of the C-O ester groups	
721	Overlapping of the CH <sub>2</sub> rocking vibration and the out-of- plane vibration of cis-disubstituted olefins	

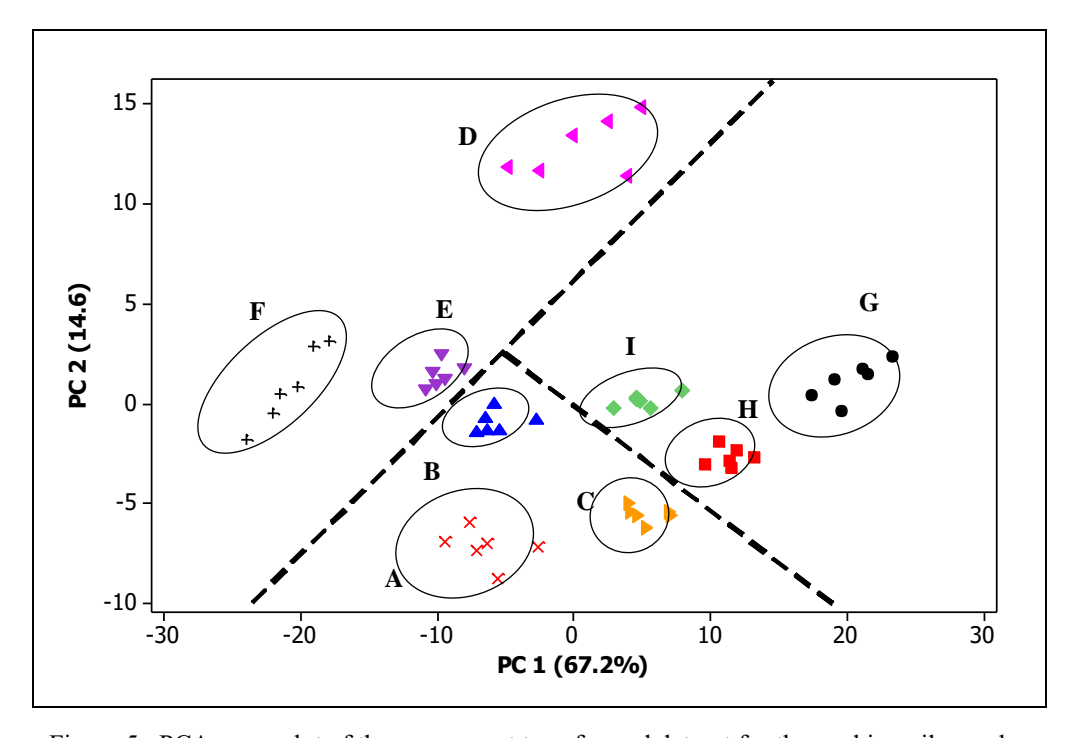


Figure 5. PCA score plot of the square root transformed dataset for the cooking oil samples

# Dzulkiflee et al: CLASSIFICATION MODEL FOR DETECTION AND DISCRIMINATION OF INEDIBLE PLASTIC ADULTERATED PALM COOKING OIL USING ATR-FTIR SPECTROSCOPY COMBINED WITH PRINCIPAL COMPONENT ANALYSIS

#### Conclusion

ATR-FTIR spectroscopy in combination with PCA can be successfully used for initial detection and discrimination of cooking oil adulterated with inedible plastic materials. Using specific IR information, PCA was able to discriminate between unadulterated and plastic adulterated cooking oil despite the dominant effect and high degree of the chemical profile similarities of TAG against the minute amount of plastic adulterants. As this study serves as an approach to simple and fast detection of inedible plastic in cooking oil, the characterisation of adulterated compounds from such activities indeed warrants further investigation.

#### Acknowledgements

The authors greatly acknowledged the funding provided by the Universiti Sains Malaysia under the Short-Term Grant Scheme (304/PPSK/61313030) which has enabled this work to be conducted.

#### References

- Almeida, D. T., Viana, T. V., Costa, M. M., Silva, C. S. and Feitosa, S., (2019). Effects of different storage conditions on the oxidative stability of crude and refined palm oil, olein and stearin (*Elaeis* guineensis). Food Science and Technology, 39 (Suppl. 1): 211-217.
- 2. Daily Express, (2014), Plastic Materials used in frying banana fritters? http://www.dailyexpress.com.my/news.cfm?NewsID=94247. [Accessed online 23 November 2020].
- 3. Ram, P., Tapos, K., Md.Saiful, I., Mohammad, A. H., Md. Mahfuzar, R. and Mahabubur, R. M. (2018). Toxic effects of plastic on human health and environment: A consequences of health risk assessment in Bangladesh. *International Journal of Health*, 6(1): 1-5.
- 4. Zuleyha, E. (2021) Melamine exposure from the weaning period causes apoptosis, inflammation and damage to the blood-brain barrier. *Journal of Chemical Neuroanatomy*, 113(1): 1-9.
- 5. Yaman, N. and Velioglu, S. D. (2019). Use of attenuated total reflectance—Fourier transform infrared (ATR-FTIR) spectroscopy in combination with multivariate methods for the rapid

- determination of the adulteration of grape, carob and mulberry Pekmez. *Foods*, 8(7): 231-233.
- Smith, R. (2019), Food fraud and adulteration detection using FTIR spectroscopy, food safety tech., https://foodsafetytech.com/feature\_article/ food-fraud-and-adulteration-detection-using-ftirspectroscopy /2/ [Access online 12 November 2020].
- 7. Meng, P., Suqin, S. and Qun, Z., (2018) a simple and portable screening method for adulterated olive oils using the hand-held FTIR spectrometer and chemometrics tools. *Journal of Food Science*, 83(6): 1605-1612.
- Bingning L., Haixia W., Qiaojiao Z., Ouyang J. and Wu, Y., (2015), Rapid detection of authenticity and adulteration of walnut oil by FTIR and fluorescence spectroscopy: A comparative study. *Food Chemistry*, 181 (1): 25-30.
- 9. Nurrulhidayah, A., Rohman, A., Amin, I., Shuhaimi, M., Khatib, A. (2013). Analysis of chicken fat as adulterant in butter using Fourier transform infrared spectroscopy and chemometrics. *Grasas y Aceitas*, 64 (4): 395-355.
- Wu, Z., Li, H. and Tu, D. (2015). Application of Fourier transform infrared (FT-IR) spectroscopy combined with chemometrics for analysis of rapeseed oil adulterated with refining and purificating waste cooking oil. *Food Analytical Methods*, 8(10): 2581-2587.
- 11. Rohman, A., Che Man, Y. B., Hashim, P. and Ismail, A. (2011). FTIR spectroscopy combined with chemometrics for analysis of lard adulteration in some vegetable oils. *CyTA Journal of Food*, 9(2): 96-101.
- 12. Skoog, D. A., West, D. M, Holler, F. M. and Crouch, S. R. (2020). Fundamentals of Analytical Chemistry: 10<sup>th</sup> Ed., Saunders College Publications. Philadelphia: pp 746-759.
- Nur Farah Dina, A., Foo K. H, Naji A. M., Wan Nur Syuhaila M. D, Mohd Rahim K., Mohammad Afiq M. H., Hasmerya M. and Dzulkiflee I., (2021). Counterfeit one hundred Malaysian ringgit banknotes discrimination using chemical imaging inspection and pattern recognition. *Australian Journal of Forensic Sciences*, 53(3); 1-15.

- 14. Asensio, R.C., Moya, M. S. A., Roja, J. M., and Gomez, M. (2009). Analytical characterization of polymers used in conservation and restoration by ATR-FTIR spectroscopy. *Analytical and Bioanalytical Chemistry*, 395(7): 2081-2096.
- Association of Official Analytical Chemists, AOAC (2019). Official Methods of Analysis., 21<sup>st</sup> edition USA: AOAC International.
- Pavia, D. L., Lampman, G. M., Kriz, G. S. and Vyvyan J. A. (2008). Introduction to spectroscopy. Cengage Learning, Stamford: pp. 31-35.
- 17. Moinuddin S. (2011). Municipal waste plastic conversion into different category liquid hydrocarbon fuel, chemistry, emission control, radioactive pollution and indoor air quality, Nicolas Mazzeo, IntechOpen https://www.intechopen.com/

- books/chemistry-emission-control-radioactive-pollution-and-indoor-air-quality/municipal-waste-plastic-conversion-into-different-category-liquid-hydrocarbon-fuel [Access online 20 February 2021].
- Lerma-García, M. J., Ramis-Ramos, G., Herrero-Martínez, J. M. and Simó-Alfonso, I. E. F. (2010). Authentication of extra virgin olive oils by Fouriertransform infrared spectroscopy. *Food Chemistry*, 118 (1): 78-83.
- 19. Rohman, A. and Che Man, Y. B. (2011). The use of Fourier transform mid infrared (FT-MIR) Spectroscopy for detection and quantification of adulteration in virgin coconut oil. *Food Chemistry*, 129(2): 583-588.